

This is to certify that the thesis entitled

NUMERICAL SIMULATIONS OF MULTIPHASE TURBULENT JETS

presented by

THOMAS GABRIEL ALMEIDA

has been accepted towards fulfillment of the requirements for the

Master of Science

degree in

Mechanical Engineering

Major Professor's Signature

01/28/2004

Date

MSU is an Affirmative Action/Equal Opportunity Institution

LIBRARY Michigan State University

PLACE IN RETURN BOX to remove this checkout from your record.

TO AVOID FINES return on or before date due.

MAY BE RECALLED with earlier due date if requested.

DATE DUE	DATE DUE	DATE DUE

6/01 c:/CIRC/DateDue.p65-p.15

NUMERICAL SIMULATIONS OF MULTIPHASE TURBULENT JETS

Ву

Thomas Gabriel Almeida

A THESIS

Submitted to
Michigan State University
in partial fulfillment of the requirements
for the degree of

MASTER OF SCIENCE

Department of Mechanical Engineering

2004

ABSTRACT

NUMERICAL SIMULATIONS OF MULTIPHASE TURBULENT JETS

By

Thomas Gabriel Almeida

The methods of direct numerical simulation (DNS) and large-eddy simulation (LES) are used to investigate the effects of heavy solid particles and evaporating droplets on planar and axisymmetric jets. The carrier gas is solved in an Eulerian frame, while the dispersed phase is computed using a Lagrangian method of tracking the droplets/particles. The DNS are carried out on a two-dimensional, droplet-laden harmonically forced jet. The effects of particle time constant, mass-loading ratio, inlet carrier gas temperature, and phase-coupling are studied and those of body forces and droplet-droplet interactions are neglected. The LES are performed on a three-dimensional, particle-laden turbulent axisymmetric jet. An a posteriori analysis of the subgrid-scale (SGS) closures used in the LES is conducted via comparison with experimental data. The effects of a stochastic SGS particle closure and inlet particle conditions are investigated by effectively turning the SGS particle closure on and off and by examining the statistics for simulations with an assumed uniform particle distribution at the inlet and those for simulations utilizing a random (Gaussian) particle size distribution. The results indicate that the proposed SGS closures implemented herein accurately capture both the effects of the particles on the carrier gas and those of the carrier gas on the particles. It is also shown that the implementation of certain physical realities, such as a non-uniform particle size distribution, can significantly increase the accuracy of the results.

DEDICATION

For my wife, Staci and my son, Gabriel.

ACKNOWLEDGEMENTS

I would like to thank those responsible for the funding of my work at Michigan State University. This research is sponsored by the U.S. Office of Naval Research under Grant N00014-01-1-0843. I am indebted to Dr. Gabriel D. Roy for his continuous support and encouragement through the course of this research. Computational resources are provided by the National Center for Supercomputer Applications (NCSA) at the University of Illinois.

I cannot express how much appreciation I have for the guidance of my advisor, Dr. F.A. Jaberi. He has been unnecessarily supportive and helpful to me from the first day I stepped into his undergraduate thermodynamics class. I would also like to thank my committee members, Dr. Z.J. Wang and Dr. N.T. Wright. They have been patient with me and vital to my growth as an engineer and researcher. Additionally, I would like to thank all of the faculty and staff at Michigan State University for producing an excellent environment for learning and research. I will be forever indebted to all of them.

Finally, I would like to thank my family and friends for always being there for me and pushing me to always do my best in everything that I encounter in life. Without the love of my wife and son, I would be lost.

TABLE OF CONTENTS

LIST OF TABLES	vi
LIST OF FIGURES	vii
NOMENCLATURE	x
INTRODUCTION	1
CHAPTER 1	
BACKGROUND	3
1.1 Particles and Isotropic Turbulence	3
1.2 Single-phase Free Jets	
1.3 Multiphase Free Shear Flows	
CHAPTER 2	
DIRECT NUMERICAL SIMULATIONS OF A PLANAR JET	15
2.1 Governing equations and computational methodology	15
2.2 Results and Discussion	
2.2.1 Nonevaporating droplets	19
2.2.2 Evaporating Droplets	
2.2.3 Interpolation	
CHAPTER 3	
LARGE-EDDY SIMULATIONS OF A ROUND JET	46
3.1 Governing equations and computational methodology	
3.2 Results and Discussion	
3.2.1 Comparison with experiment	50
3.2.2 Additional physical Observations	60
CHAPTER 4	
CONCLUSIONS	72
REFERENCES	77

LIST OF TABLES

Table 1. Physical parameters	19
Table 2. Two-way coupling cases	26
Table 3. Evaporative case descriptions	35
Table 4. Physical parameters	50
Table 5. Case summary	51
Table 6. Sample percent error for mean axial velocity at jet centerline, ucl	53
Table 7. Sample percent error for mean axial velocity, u _m	54
Table 8. Sample percent error calculations for u _{rms}	57
Table 9. Sample percent error calculations for Tu	58

LIST OF FIGURES

_	1. Vorticity magnitude and particle locations, one-way coupling. (a) $\tau_p = 0.1$, (b) $\tau_p = 1.0$ and (c) $\tau_p = 10.0$	l
Figure	2. Particle inertia effects on integrated particle number density22	2
Figure	3. Particle number density transverse profiles at $x/h = 8$. Note the vertical shift applied to the $\tau_p = 1.0$ and the $\tau_p = 100.0$ cases	3
Figure	 4. Particle dispersion as a function of injection. (a) uniform over 4h, (b) uniform over 2h and (c) at shear layer over 2Δy	4
Figure	5. Particle injection effects on particle dispersion. The x/h = 3 data is shifted up by 300	5
Figure	6. Effect of particle time constant on jet growth rate. (a) whole field and (b) regression analysis of self-preserving region	7
Figure	7. Particle centerline axial velocity versus particle size	8
Figure	8. Effect of mass loading on jet growth rate. (a) whole-field and (b) regression analysis of self-preserving region	9
Figure	9. Centerline axial velocity profiles as a function of mass-loading30)
Figure	10. Reynolds stress profiles versus mass-loading. (a) axial variation at the shear layer and (b) transverse variation at x/h=6	1
Figure	11. Production of TKE profiles versus mass loading. (a) axial variation at the shear layer and (b) transverse variation at x/h = 6	2
Figure	12. Temperature effects for two-way coupling at centerline	4
Figure	13. Two-way coupling temperature effects on velocity profiles at x/h=63	4
Figure	14. Jet half-width versus coupling (T=600) (a) actual growth and (b) linear regression of the linear portion of the growth rate	6
Figure	15. Centerline axial velocity profiles as a function of coupling (T=600)3	7
Figure	16. Reynolds stress profiles for different coupling (T=600). (a) axial variation at shear layer and (b) transverse variation at x/h=6	8

Figure	17. Production of TKE profiles for different coupling (T=600). (a) axial variation at the shear layer and (b) transverse variation at $x/h = 6$
Figure	18. Temperature variation in the axial direction for different coupling cases
Figure	19. Density and mass fraction of vapor variation in the axial direction for different coupling cases
Figure	20. Transverse variation of temperature and density42
Figure	21. Development of the probability distribution function of particle mass43
Figure	22. Eulerian averaged particle mass and Reynolds stress profiles at various downstream locations
Figure	23. Temperature profiles versus interpolation schemes
Figure	24. Jet growth rate as a function of interpolation scheme
Figure	25. Vorticity magnitude and particle distribution
Figure	26. Centerline mean axial velocity versus downstream location53
Figure	27. Axial velocity profiles at (a) $x/D = 5$ and (b) $x/D = 12.5$
Figure	28. Spatial Development of Axial Velocity Profiles at x/D = 2.5, 5 and 12.5
Figure	29. Radial profiles of RMS of axial velocity at (a) x/D = 5 and (b) x/D = 12.5
Figure	30. Radial profiles of turbulence intensity at $x/D = 5$ and 12.558
Figure	31. Mean centerline axial velocity of single- and two-phase flow59
Figure	32. Radial profiles of mean axial velocity at x/D = 7.560
Figure	33. Particle number density versus downstream distance61
Figure	34. Carrier gas and particle velocity versus radial position at (a) x/D=2.5, (b) x/D=5.0 and (c) x/D=12.561
Figure	35. Correlation between particle axial velocity and particle mass at different downstream locations

Figure 36. Particle mass versus radial position at different downstream locat	ions63
Figure 37. Particle mass and number density radial variation at different axial locations	64
Figure 38. Probability distribution function of particle mass	65
Figure 39. Axial variation of correlation between particle and carrier gas velocities	66
Figure 40. Radial variation of correlation between particle and carrier gas velocities	68
Figure 41. Particle temperature as a function of particle mass	69
Figure 42. Mean axial velocity versus radial position for varying average particle inertia at (a) $x/D = 5$ and (b) $x/D = 12.5$	70
Figure 43. Mean axial velocity (a) versus axial position at the centerline and (b) versus radial position at x/D = 7.5	71

NOMENCLATURE

B_{M}	mass transfer number
C_p	specific heat at constant pressure of fluid
C_p D	jet diameter
$d_p \ E$	particle diameter
Ė	total energy
f_{l}	coefficient related to particle drag
f_2	coefficient related to particle heat and mass transfer
f_3	coefficient related to particle heat and mass transfer
$J_i^{ m{lpha}}$	mass flux of species α in i th direction
K	thermal conductivity
Ma	Mach number
m_p	mass of particle
N_s	number of species
Pr	Prandtl number
p	pressure
q_i	heat transfer in ith direction
R^o	universal gas constant
R	molecular weight gas constant
Re	Reynolds number
r	radial position
r_o	jet radius
S_e	energy source term
S_{ui}	momentum source term in ith direction
$S_{ ho} T$	mass source term
	fluid temperature
T_p	particle temperature
Tu	turbulence intensity
t	time
u_i	i th component of fluid velocity vector, U
u_i	deviation from the mean velocity in i th direction
u_{cl}	centerline axial velocity
u_m	mean axial velocity
$\frac{u_{rms}}{}$	root-mean-square of axial velocity
u'v'	Reynolds stress
v_i	i th component of particle velocity vector, V
W_{α}	molecular weight of species α
X_i	i th component of Lagrangian coordinate system
x_i	i th component of Eulerian coordinate system
Y_{α}	mass fraction of species α

Greek Symbols

- α_2 ratio of specific heat of the particle to that of the fluid
- δ_{ii} Kronecker delta
- δV Eulerian differential volume
- δx grid spacing
- γ ratio of specific heats of the fluid
- η coefficient related to droplet evaporation
- μ fluid viscosity
- ρ fluid density
- ρ_p particle density
- σ_{ij} Newtonian fluid stress tensor
- τ_p particle time constant

INTRODUCTION

Multiphase flows occur in a wide range of engineering applications. Ink jet printers, internal combustion engines and fire prevention systems are obvious examples of physical situations for which the understanding of multiphase transport phenomena are very important. Due to the range of applicability of these flows, scientists and engineers continue to work on these problems with fervor. This work is focused on a specific class of multiphase flows, that of dilute turbulent free shear flows laden with a dispersed medium, either solid particles or evaporating droplets. There exists an underlying difficulty in dealing with such flows for various reasons. For experimentalists, one such difficulty is resolving the properties of both (or all) phases involved. For example, to use phase-Doppler anemometry (PDA) or particle imaging velocimetry (PIV) to capture the velocity field of both the carrier gas and the dispersed phase would require some method of differentiating between the seeding particles and the actual dispersed particles, such as a separation of scales. Analytically, the amount of simplifications required to make the governing equations tractable would greatly reduce the range of applicability of said equations. One of the more promising methods of predicting turbulent multiphase flows is the use of computational methods. While there are limitations to the use of numerical methods, the benefits seem to outweigh the costs. The long-range impact of this work is to aid in the development of subgrid-scale (SGS) closures for the large-eddy simulation (LES) simulation methods of computing multiphase flows. The calculations performed herein are direct numerical simulations (DNS), utilizing a particle-source-in-cell (PSIC) methodology. While some critics argue that this is not true DNS because the smallest scales of the flow around each individual particle or droplet are not resolved, the careful

analysis of the results indicates that the assumptions and correlations used are indeed valid.

In order to develop accurate closure models for LES, one must establish an effective way of validating the proposed models. This work is an effort both to understand the complex physics associated with multiphase turbulent flows and to develop a usable database of DNS results. Once the database is established, one can use those results to develop closures for various turbulence modeling techniques that are robust enough to accurately predict the effects of adding solid particles or evaporating droplets to various turbulent flows.

To this end, the author has conducted numerous numerical experiments of two-dimensional, harmonically-forced planar jets laden with heavy solid particles or evaporating droplets. The code utilized is a fully-compressible, three-dimensional, density-based research code. The simulations discussed herein are 'pseudo-two-dimensional', for the longitudinal depth of the planar jet is small enough to force the variations in the z-direction to zero. Eventually, this same code will be utilized to run large-scale, three-dimensional numerical experiments of fully turbulent planar jets laden with particles or droplets. The details of the simulation parameters will be discussed in more detail in sections to follow.

CHAPTER 1 BACKGROUND

To better understand the underlying physics of multiphase free shear flows, one must first understand the 'building blocks' of multiphase turbulent flows, i.e., first consider single-phase free shear flows and modulation of isotropic turbulence by particles separately, then combine the two. Another important aspect of this work is the inclusion of evaporative effects. While understanding evaporation may be fairly straightforward, the problem of understanding how evaporation will affect transitional and turbulent flows has more intrinsic difficulties associated with it.

1.1 Particles and Isotropic Turbulence

Elghobashi and Truesdell (1993) investigated the effects of dispersed, small, solid, spherical particles on decaying homogeneous turbulence, noting a "selective spectral redistribution" of turbulent kinetic energy and an increase in the decay rate of turbulence. The particles increase the turbulent kinetic energy for lower wave numbers and increase it for higher ones. Yang and Lei (1998) studied the effects of turbulence scales on particle settling velocity by considering homogeneous isotropic turbulence laden with particles. They noted that low wave number components affect the particle accumulation, while the small wave number components do not. However, they also found that the settling rate depends on the large scales of turbulent motion. Boivin, Simonin and Squires (1998) used direct numerical simulation (DNS) to study turbulence modulation due to particles, and found that they tend to dissipate the kinetic energy. The degree to which they affect the flow was found to scale with the mass loading. They also noted that the particles distort

the energy spectra (as opposed to attenuating or amplifying uniformly). Upon investigation of particle size effects, they found that the effects on low wave number energy region were independent of particle size, but that at high wave numbers, the larger particles damp the turbulence and the smaller ones amplify it. Ooms and Jansen (2000) also studied the effects of particles on homogeneous, isotropic turbulence. They give a reasonable physical argument as to why the size of the particle can lead to different turbulence modulation. They state that, if the volume fraction is held constant, smaller particles have more surface area than large ones and thus cause more friction, which leads to a larger suppression of fluid turbulence. They also give this as a reason to use caution when using point-source particle approximations.

Jaberi (1998) conducted a study of fluid-particle thermal interactions in a particle-laden homogeneous turbulent flow. His findings indicate that the temperature of both the carrier gas and the dispersed phase are dependent upon various properties, such as the particle time constant and the mass-loading ratio. The specific intent was to determine the effects on the temperature fields. He found that increasing the mass loading causes the p.d.f. of particle temperature to deviate from a Gaussian distribution. Mashayek and Jaberi (1999) collaborated to study isotropic turbulence and particle dispersion, noting that the particle velocity auto-correlation coefficient drops off more sharply with lower mass loading ratios. They also noted that the pressure-dilatation correlation is significantly damped by the presence of particles.

1.2 Single-phase Free Jets

One specific flow of particular significance to this work is that of free jets. Free jets, both planar and round, have been the focus of much research. The general features of the turbulence fields in such flows are well-established. Hinze (1975), Pope (2000), Bernard and Wallace (2002) and others have discussed these flows in detail, noting the general characteristics of the self-preserving portion of the flow. It has been shown that the jet half-width grows linearly and the centerline mean velocity decays proportional to the inverse of the square root of the axial position. The self-preserving nature of the jet leads to the formulation of a non-dimensional velocity profile, which is unchanging. It has also been shown that the root-mean-square (RMS) of velocity fluctuations and the 'Reynolds-stress' profiles are self-similar as well. The development of free shear flows has been attributed to instabilities which are controlled by the Kelvin-Helmholtz mechanism.

More recently, researchers have turned their focus to determining the specific causes and physical explanations for the observed behavior. The instabilities which cause a jet to develop have been investigated in detail by Hsiao and Huang (1990). Their work involved a plane jet that they subjected to acoustic forcing. They investigated the growth of instabilities and the velocity correlations within the jets. They found both the streamwise and transverse fluctuating components to be important to the development of said instabilities. Their work is of particular relevance to this work because they used experimental methods to force the jet harmonically, similar to the way in which the jets in this work are numerically forced. They found that small perturbations caused the jet to develop much more rapidly than unforced jets, and that the structure of the flow was

greatly modified. One finding of particular significance was that the fluctuating velocity profile along the inside of one shear layer displayed a convenient way to see vortex merging and saturation. This helped them conclude that the harmonic forcing adds energy to the fundamental frequency to the point of saturation and then adds to the first subharmonic, then the second, etc. This was also shown in the development of the half-width of the jet, which showed plateaus near the harmonics.

Stanley and Sarkar (1997) studied two-dimensional shear layers and jets, noting the impact that external forcing has on the jet development. Their work aided the author of this work in choosing the harmonic forcing used (as described in Chapter 2). They found that, although the down-stream growth was nearly unaffected by forcing at the inlet, the near-field was modified. They reported some interesting result related to the symmetry of 'weak' and 'strong' jet flows due to forcing. The simulations performed herein would be classified as strong. Stanley and Sarkar found that the sinuous (antisymmetric) forcing of the jets lead to a more realistic velocity field.

Another work of interest was that of Kennedy and Chen (1998). They studied the effects of temperature on the growth and stability of free jets and found that cold jets tended to be significantly more stable than isothermal or hot jets. They attribute much of this observation to increased compressibility. They also indicated a modification of mean velocity profile, where the cold jets profile were 'more narrow' and had a "more gradual taper of velocity" than their isothermal and hot counterparts. They also noted that the transverse location of the vorticity maxima decreased with decreasing temperature and

the value of that maxima increased. These are explained by Colucci (1994) investigated the linear stability of shear flows under density-stratified conditions. He found that decreasing the density of the high-speed stream would increase instabilities, thereby increasing turbulence and mixing. He also found that either increasing or decreasing the density of the stream would stabilize the low-wave numbers. Another important finding was that the convective wave speed is biased towards the higher density stream. He also investigated the effects of 'density spikes' at the region of highest shear, noting that decreasing the density of the shear zone damps the instabilities, thus slowing the growth rate of the jet.

1.3 Multiphase Free Shear Flows

Recent advances in experimental methods and computational power have given researchers more access to multiphase flow analyses. Whole texts have been authored on this subject (e.g., Fan and Zhu (1998), Sommerfeld, Tsuji and Crowe (1997)). Yet, there is still room for advancement of the ever-broadening field. Crowe, Chung and Troutt (1988) used numerical and experimental evidence to show that particle dispersion in free shear flows is controlled by large-scale vertical structures, and not so much by diffusion (particle concentration gradients). They also classified particles by their aerodynamic response time (as compared to the fluid characteristic time scale) into three categories: small, intermediate and large particles. They also mention the effects of forcing a jet on the particle dispersion by regularizing the vertical structures, which increases the dispersion of smaller particles.

Hansell, Kennedy and Kollmann (1992) used numerical methods to study the effects of individual forces on particle dynamics. They found that, under certain circumstances, the omission of forces beyond those of the drag, such as Bassett history and virtual mass, could lead to errors in droplet dispersion on the order of 25%. They discuss the differences between the vaporizing and non-vaporizing droplet models. The findings are useful but only pertain to droplet dispersion, not to the two-way coupling effects of the particles on the carrier gas. The additional forces involved in particle dynamics may have a significant effect on dispersion, but the effects on the carrier gas properties have yet to be determined with great accuracy.

Eaton and Fessler (1994) studied preferential concentration of particles due to turbulence. They found that the coherent turbulent structures are still present in particle-laden flows, but that they are modified. Once again the particle concentration was found to be determined by the large-scale structures in the flow. They found that the size of the particle has an important effect on the concentration; neither large nor small particles will preferentially concentrate, while intermediate-sized particles will. The preferential concentration of droplets in particular can have drastic effects on the evaporation and burning of fuels. For this reason, the size of the droplets should be carefully considered before designing a system involving evaporation.

Mashayek (1998a, 1998b) used DNS to study the droplet size, vapor mass fraction and temperature field in droplet-laden, forced, low-Mach number turbulence. An important finding was that the addition of solid particles to homogeneous shear flows causes a

decrease in turbulent kinetic energy and an increase in the anisotropy of the flow, but that evaporation can effectively decrease that anisotropy. He also found that increasing the mass-loading ratio causes the temperature of the carrier gas to decrease more initially and then increase more at longer times. What can be seen to occur in temporal variations here may be seen in spatial development in anisotropic flows. This is attributed to the increased temperature difference between phases, and the increased heat capacity of the larger droplets. He also found the probability distribution functions of the particle diameter to be skewed towards smaller droplets. The vapor mass fraction was found to become saturated at long times. He also noted that the evaporation rate is higher in regions of high shear, which then indicates that the Reynolds number is a very important parameter governing droplet vaporization.

Experimental results for a particle laden round jet were reported and analyzed by Longmire and Eaton (1992). The visualizations offered in their work are fascinating. They too found that the large-scale vortices controlled the particle dispersion. The jet that they studied was acoustically forced. They found that the total particle number density decreased in the axial direction, and that the number of particles in low-concentration areas increased with axial distance from the inlet. They also noticed that the slightly smaller particles tended to accumulate in regions between the large vortices, lending to periodic peaks and troughs in particle number density corresponding to the forcing frequency. Round jets and particle dispersion were the focus of Kennedy and Chen (1998). In an effort to simplify the theory of particle-laden shear flows, they suggested

that particles with Stokes numbers less than unity should behave like fluid particles and therefore self-preserving laws should hold for these cases.

Several different models for evaporation models were compared by Miller, Harstad and Bellan (1998). They fund that the Langmuir-Knudsen model was the most accurate (and thus was chosen as the formulation for this author's work). The work is a very thorough and direct synthesis of various important aspects related to droplet-laden shear flows. They also found that the constant property assumption was an accurate one for temperatures calculated at the boiling temperature. Armenio and Fiorotto (2001) studied the importance of the different forces acting on particles. The intent was to determine which, if any, could be neglected in favor of computational efficiency. They found that the most important force is that due to drag and that added mass effects are always negligible, but that Bassett history forces may be important in certain flow regimes. They are definitely not important to particle dispersion, though.

Armenio, Piomelli and Fiorotto (1999) and Bellan (2000) have investigated some of the important issues related to turbulence modeling and multiphase flows. Both discuss the state of the art and give more suggestions for further work. Miller and Bellan (2000) contribute even more to the underlying theme of computational modeling of multiphase flows. All of these researchers found that the effects of the sub-grid scales on various particle properties are significant. Specifically, Miller and Bellan (2000) mention that there may be a need to model some of the subgrid scale fluctuations to accurately predict the particle dispersion and droplet evaporation. Boivin, Simonin and Squires (2000) also

discuss some of the issues related to the LES of multiphase flows. They are careful to mention the restrictions on *a priori* testing, but they also found their models to be fairly accurate for gas-solid flows (note that there is still much room for studies involving evaporating droplets).

One of the more promising methods of doing so is the subset of numerical methods termed large eddy simulations (LES). As Bellan (2000) described, there remains a seemingly inexhaustible amount of work to do on the development of LES closures to accurately model the interaction between the small-scale turbulence of the carrier fluid phase and the dispersed phase. While there are a steadily growing number of studies involving the development and verification of SGS models using a priori studies applied to direct numerical simulation (DNS) results, there is a noticeable deficit in the area of validation of LES results via a posteriori analysis of numerical results by comparison with experimental data. To ensure the accuracy of a given model, both verification and validation studies should be conducted as suggested by Boivin, Simonin & Squires (2000). Their work mostly concerns the spectral analysis of DNS and various LES models. The importance of correlation with experimental data as well as with DNS data cannot be overlooked. While there have been several experimental studies (e.g., Longmire and Eaton (1992) and Schreck and Kleis (1993)) on the subject of particleladen flows, many of these deal with the far-field of as yet prohibitively high Reynolds number flows and/or do not report results for both the carrier and dispersed phases concurrently, and thus are insufficient to determine the direct effect of the particles on the carrier gas and vice versa. The goal of LES is, of course, to be able to predict the near and

far flow fields of increasingly high Reynolds numbers, but it seems to be more prudent to focus first on accurately predicting the near field of lower Reynolds number flows before moving on to the far field of high Reynolds number flows.

Armenio, Piomelli and Fiorotto (1999) investigated the effects of the SGS on particle motion. Their work indicates that using a filtered velocity field to advance the particles can lead to serious inaccuracies; thus the importance of the SGS closures is emphasized. In Chapter 3, the importance that they refer to will be investigated. Miller and Bellan (2000) conducted a thorough a priori analysis of the SGS using DNS results for a transitional mixing layer, and they also concluded that neglecting the SGS velocity fluctuations in LES might lead to gross errors in the prediction of the particle drag force. This, in turn, will lead to errors in both the carrier-phase and the dispersed-phase. Miller (2001) went on to investigate the effects of solid particles on an exothermic reacting mixing layer. He found that the particles were preferentially concentrated in the highstrain braid regions of the mixing layer, which can lead to local flame extinction. Additionally, several researchers have used DNS methods to gain a better understanding of multiphase flows. Mashayek (1998a, 1998b) and Jaberi (1999) noted that the presence of particles effectively decreases the turbulent kinetic energy while increasing the anisotropy of homogeneous turbulent shear flows. These effects were shown to be magnified by increasing either the mass-loading ratio or the droplet time constant. They also found that the autocorrelation coefficient of the velocity of the carrier gas in an isotropic two-phase flow increases with an increase in mass-loading ratio. Jaberi (1998) and Jaberi and Mashayek (2000) studied particle temperature in homogeneous

turbulence. They noted that the temperature intensity decreases with increasing particle time constant, thermal diffusivity and Prandtl number. Also of great significance was the finding that velocity coupling is not sufficient to resolve the physics of non-isothermal two-phase flows. It is necessary to include thermal coupling effects as well. Additionally, their results indicate that increasing the mass-loading ratio causes the carrier fluid temperature fluctuations to increase (further causing a decrease in the decay rate of fluid temperature in decaying isotropic turbulence) and increasing the particle time constant increases the temperature difference between the particles and the carrier fluid.

Chapter 3 will offer evidence that the SGS closures discussed and implemented herein are both applicable and accurate. This is accomplished through correlation with the experimental data obtained by Gillandt, et al. (2001). They have generated phase-Doppler-anemometry (PDA) results for a moderately high Reynolds number round jet laden with heavy particles. The desire to improve the applicability of LES to multiphase flows is complemented by the current limitations of experimental methods of flow measurement. The PDA system described can measure the velocities of both the carrier gas and the particles, but the particles must be much larger than the tracers (to offer a definitive separation of scales). This results in a description of a flow that involves particles larger than those that may be seen in some industrial applications. In contrast, the LES methods described herein may be used for various particle sizes and Reynolds numbers at no more expense than the original studies. This work is somewhat similar to the investigation of a slit-jet by Yuu, Ueno, and Umekage (2001). However, an additional emphasis is placed on the comparison of the LES with and without the SGS models to the

experiment. Also, there are important physical differences between planar and axisymmetric free jets.

CHAPTER 2 DIRECT NUMERICAL SIMULATIONS OF A PLANAR JET

2.1 Governing equations and computational methodology

The formulation used for this study is similar to that of Miller and Bellan (1999). The carrier gas phase is treated in an Eulerian frame, and a Lagrangian frame of reference is used for the dispersed phase (either solid particles or liquid droplets). While there has been some discussion and research in the area of Eulerian-Eulerian frames versus Eulerian-Lagrangian frames, the latter has been chosen for simplicity of implementation and lack of modeling requirements. The two-way coupling effects of the carrier gas on the droplets and the droplets on the carrier gas are due to the inclusion of each particle as a point source or sink of mass, momentum, and energy. This is commonly referred to as the particle-source-in-cell (PSIC) or particle-in-cell method. The equations are derived under the assumptions of calorically perfect species (carrier gas and evaporate), no body forces (e.g., gravity) and the dispersed phase volume fraction much less than unity. The non-dimensional Eulerian equations for continuity, momentum, energy and scalar (evaporate) are

$$\frac{\partial \rho}{\partial t} + \frac{\partial \rho u_i}{\partial x_i} = S_{\rho} \tag{2.1}$$

$$\frac{\partial \rho u_i}{\partial t} + \frac{\partial \rho u_i u_j}{\partial x_j} = -\frac{\partial P}{\partial x_i} + \frac{1}{\text{Re}} \frac{\partial \sigma_{ij}}{\partial x_j} + S_{ui}$$
(2.2)

$$\frac{\partial \rho E}{\partial t} + \frac{\partial \rho E u_i}{\partial x_i} = -\frac{\partial P u_i}{\partial x_i} + \frac{1}{\text{Re}} \frac{\partial u_j \sigma_{ij}}{\partial x_i} - \frac{1}{(\gamma - 1)Ma^2 \text{Re Pr}} \frac{\partial q_i}{\partial x_i} + S_E$$
 (2.3)

$$\frac{\partial \rho Y_{\alpha}}{\partial t} + \frac{\partial \rho Y_{\alpha} u_{i}}{\partial x_{i}} = -\frac{1}{\text{Re Pr } Le_{\alpha}} \frac{\partial J_{i}^{\alpha}}{\partial x_{i}} + \dot{\omega}_{\alpha}$$
(2.4)

The pressure, gas constant, Newtonian shear stress, heat flux, mass flux, total energy and enthalpy are defined by

$$P = \frac{1}{\gamma Ma^2} \rho RT \tag{2.5}$$

$$R = R_u \sum_{\alpha} \frac{Y_{\alpha}}{W_{\alpha}} \tag{2.6}$$

$$\sigma_{ij} = \mu \left(\frac{\partial u_i}{\partial x_j} + \frac{\partial u_j}{\partial x_i} - \frac{2}{3} \delta_{ij} \frac{\partial u_k}{\partial x_k} \right)$$
(2.7)

$$q_{i} = -\mu \left(c_{p} \frac{\partial T}{\partial x_{i}} + \sum_{\alpha} \frac{h_{\alpha}}{Le_{\alpha}} \frac{\partial Y_{\alpha}}{\partial x_{i}} \right)$$
(2.8)

$$E = \frac{1}{(\gamma - 1)Ma^2} \sum_{\alpha} h_{\alpha} Y_{\alpha} - \frac{P}{\rho} + \frac{u_i u_i}{2}$$
(2.9)

$$h_{\alpha} = h_{\alpha}^{0} + c_{p\alpha}T \tag{2.10}$$

It should be noted that for a perfect binary mixture (of the carrier gas and the evaporate), $\alpha = 1$, $\dot{\omega} = S_{\rho}$. The Lagrangian equations for the droplets are defined by

$$\frac{dX_i}{dt} = v_i \tag{2.11}$$

$$\frac{dv_i}{dt} = \frac{f_1}{\tau_p} \left(u_i - v_i \right) = \frac{F_i}{m_p} \tag{2.12}$$

$$\frac{dT_p}{dt} = \frac{\eta f_2}{\tau_p} \left(T - T_p \right) + \frac{L_v}{m_p c_L} \frac{dm_p}{dt} = \frac{Q_{conv} + L_v \dot{m}_p}{m_p c_L}$$
(2.13)

$$\frac{dm_p}{dt} = -\frac{m_p f_3}{\tau_p} \ln(1 + B_M) = \dot{m}_p$$
 (2.14)

The subscript p indicates the droplet/particle property, and the fluid properties are interpolated to the droplet position. The value of f_l is empirically evaluated for the Stoke's drag, based on the particle slip and blowing Reynolds numbers, Re_{sl} and Re_b. Similarly, f_2 and f_3 are functions of the droplet properties; both involving heat and mass transfer properties, such as the Nusselt number (Nu), Prandtl number (Pr), Sherwood number (Sh) and Schmidt number (Sc). L_v, c_L and B_M are the droplet heat of vaporization, heat capacity and mass transfer number, respectively, and the particle/droplet time constant is defined as

$$\tau_p = \frac{\operatorname{Re} \rho_p d_p^2}{18\mu} \tag{2.15}$$

Evaporation is taken into account via the Langmuir-Knudsen evaporation model, which takes into account both equilibrium and non-equilibrium effects, and the traditional 'D' law' of Godsave and Spalding is also implemented. Finally, the two-way coupling effects are taken under consideration through the use of the source terms which, for mass, momentum and energy, are defined as

$$S_{\rho} = -\frac{1}{\delta V} \sum_{np} \dot{m}_{p} \tag{2.16}$$

$$S_{ui} = -\frac{1}{\delta V} \sum_{np} \left(F_i + \dot{m}_p v_i \right) \tag{2.17}$$

$$S_{E} = -\frac{1}{\delta V} \sum_{np} \left(\frac{Q_{conv}}{(\gamma - 1)Ma^{2}} + v_{i}F_{i} + \dot{m}_{p} \left(\frac{h_{v,s}}{(\gamma - 1)Ma^{2}} + \frac{v_{i}v_{i}}{2} \right) \right)$$
(2.18)

These source terms are evaluated for each individual particle and then summed over a finite Eulerian volume, δV .

The carrier gas Eulerian equations are temporally solved via a second-order, modified MacCormack technique (predictor-corrector), and the spatial derivatives are calculated using a sixth-order compact finite differencing scheme. The dispersed phase equations are calculated via traditional Eulerian time stepping. The carrier gas properties are interpolated to the droplet position via two methods, first-order linear and fourth-order Lagrange polynomial. The accuracy of the linear interpolation was determined to be sufficient to resolve the interaction between phases, and thus was used in the great majority of simulations (see Section 2.2).

The jet inlet velocity profile chosen was tangent hyperbolic and the jet was subjected to random-phase harmonic forcing at the shear layer in the transverse (y) direction. The forcing energy peak was set at 5% for each of five frequencies, the harmonic, one superharmonic and three sub-harmonics. Each harmonic had a randomly generated phase angle between 0 and $\pi/2$, which was changed each time step. The phase angles applied to the top shear region were different than those applied to the bottom region. The inlet boundary condition was derived from the work of Poinsot and Lele (1992). The y-direction boundary conditions (BCs) were chosen to be zero-derivative free-stream, the z-direction BCs were periodic, and the non-reflecting outlet boundary condition used was that of Rudy and Strikewerda (1980).

The statistical properties were averaged over three pass-over times, where the pass-over time is given by

$$t_{pass} = \frac{x_{\text{max}}}{\left(u_{jet} + u_{co}\right)/2} \tag{2.19}$$

Convergence was confirmed via comparison between the mean and RMS properties at two different times, noting less than 1% difference. The jet was given one and a half pass-over times to develop initially before the averaging was started. In different simulations, various parameters were varied. Specifically, the particle time constant, the carrier gas temperature, the mass loading ratio and the 'coupling' were treated as independent variables. The mean and RMS of axial velocities, temperature, density and mass-fraction of species, as well as the Reynolds stress and production term of turbulent kinetic energy were all calculated as dependent variables for this study.

2.2 Results and discussion

Some of the physical parameters for the numerical simulations are given in Table 1. Note that these simulations are chosen to emulate a planar jet of air laden with droplets of decane. The parameters can easily be modified to more closely match any of several physical configurations. In the following sections, more parameters are discussed as they relate to the particular scenario.

Table 1. Physical parameters

Carrier Fluid	Air
Dispersed Phase	Decane Droplets
Jet Reynolds Number	3165
Jet Mach Number	0.291
Prandtl Number	0.75

2.2.1 Nonevaporating Droplets

The following section is primarily concerned with how the carrier gas affects the nonevaporating droplets. For these simulations, all of the source terms were set to zero, but the droplet equations were solved. The droplets (or particles) are therefore not allowed to have any effect on the carrier gas. The gas 'pushes' the particles around without 'feeling' any reciprocal force.

The effects of particle inertia on particle dispersion are shown in Figure 1. Expectedly, it is observed that the small particles tend to follow the flow of the carrier gas, while the large ones tend to move at their own inlet/initial velocity (less affected by the carrier gas). For a more quantitative understanding of particle dispersion, the particle number density has been compared for different particle time constants in Figures 2 and 3.

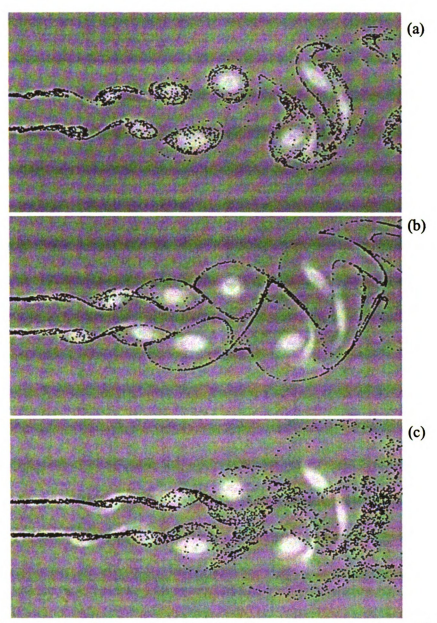


Figure 1. Vorticity magnitude and particle locations, one-way coupling. (a) $\tau_p=0.1$, (b) $\tau_p=1.0,$ and (c) $\tau_p=10.0$

Figure 2 shows that the number of particles integrated over the y-direction is relatively constant for high inertia particles, erratic for intermediate size particles, and approximately harmonic (farther downstream of the jet inlet) for small particles. Again, this is fortuitous in that the flow is harmonically forced, and the small particles behave like fluid particles. Figure 3 shows the transverse variation of particle number density as

it relates to particle size. The striking characteristic of the flow observed in this plot is what we call 'local particle dispersion'. Both the small and the large particles have regions of high particle dispersion, while the intermediate size particles ($\tau_p = 1.0$) clearly shows minimal local particle dispersion in the narrow width and high peaks of the high particle density regions. For the other particles, the high particle density regions are broader and, on average, less dense. This has important implications when evaporative and/or reactive particles are considered.

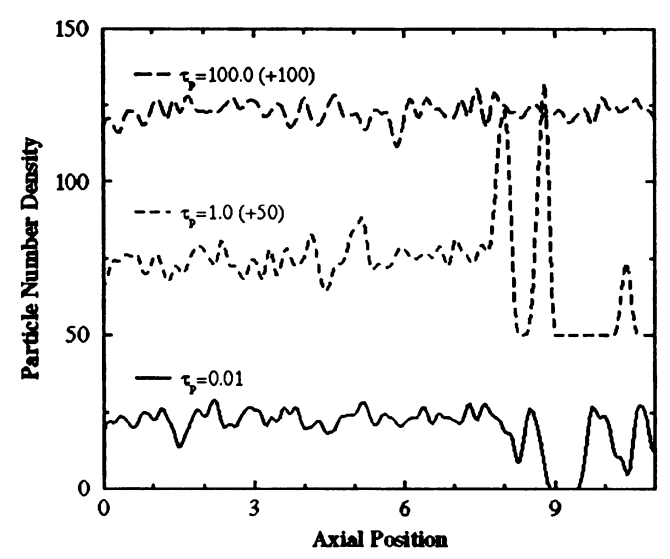


Figure 2. Particle inertia effects on integrated particle number density. The curves for $\tau_p = 1.0$ and 100 are shifted upward for clarity.

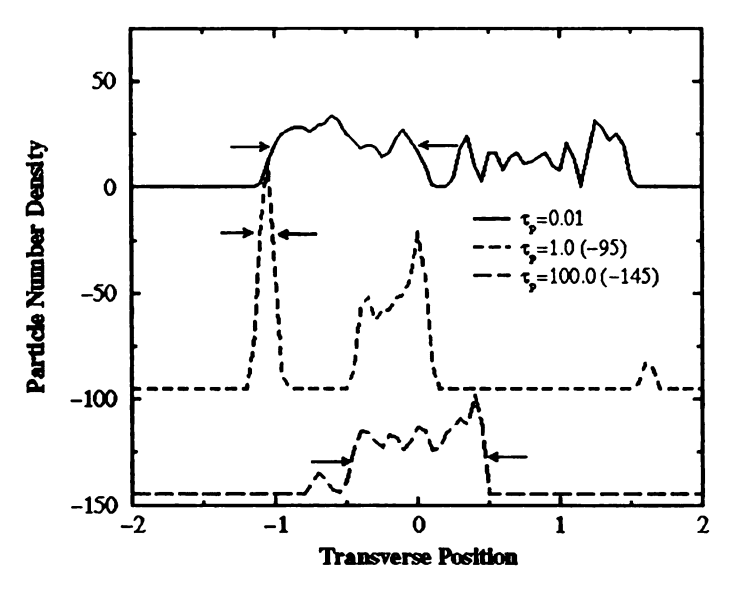


Figure 3. Particle number density transverse profiles at x/h = 8. Note the vertical shift applied to the $\tau_p = 1.0$ and the $\tau_p = 100.0$ cases

The effects of particle injection are shown in Figures 4 and 5. Notice that the downstream behavior of the particles with $\tau_p = 1.0$ is basically independent of particle injection location. Specifically, in Figure 5, the particle number density plots show that at downstream locations of $x/h \ge 9$, the local particle dispersion is approximately constant for the given particle size. This statement only holds true for one-way coupling, as the particle concentration in the shear layer affects the growth or decay of instabilities in two-way coupling cases and the results are sensitive to inlet/initial particle distribution.

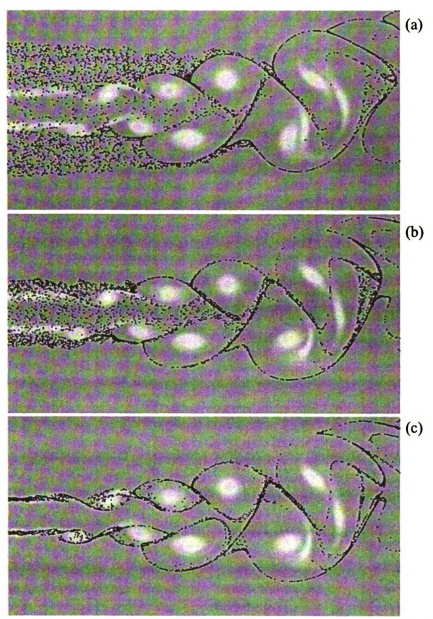


Figure 4. Particle dispersion as a function of injection. (a) uniform over 4h, (b) uniform over 2h, and (c) at shear layer over $2\Delta y$. $\tau_p=1.0$ in all cases.

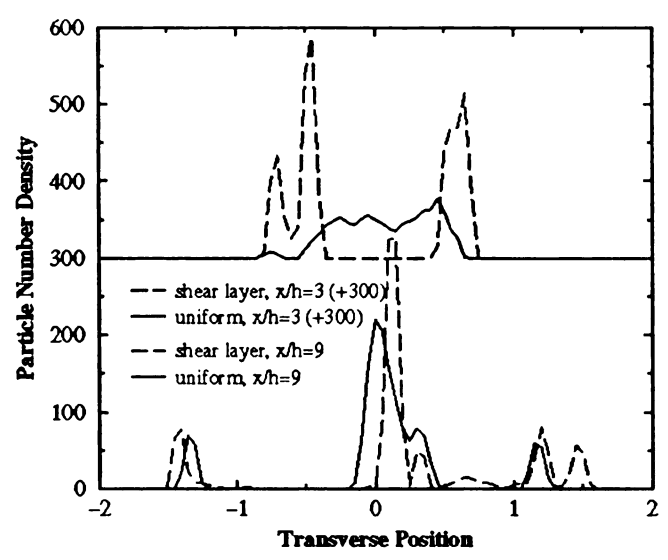


Figure 5. Particle injection effects on particle dispersion. The x/h = 3 data is shifted up by 300.

For the two-way coupling cases considered in this section, the energy and momentum source terms are affecting the carrier gas, however the droplets are still non-evaporating. This allows for realistic physical simulations with two-way coupling effects present, but removing the complexities due to evaporation. The effects of particle size, mass loading and carrier gas temperature were investigated in detail. The outline of the different cases and their parameters is given in Table 2. Case 7 was conducted as a reference to verify the modifications due to the temperature-dependency of density and viscosity, and to separate from those the effects of the particles as 'temperature sinks' on the carrier gas field. The results of cases 1, 2 and 3 aid in the understanding of the effects of particle size on various turbulent properties. Cases 2, 4, 5 and 6 were designed to show the effects of mass-loading (or initial particle number density). Cases 2, 7 and 8 show the effects of varying the carrier gas temperature.

Table 2. Two-way coupling cases

Case	$ au_{ m p}$	фт	T
1	0.1	0.2184	293
2	1.0	0.2184	293
3	10.0	0.2184	293
4	1.0	0.2908	293
5	1.0	0.3637	293
6	1.0	0.4365	293
7	1.0	0.4472	600 (dTp/dt=0)
8	1.0	0.4472	600

Figure 6 shows the jet half-width growth rate for different particle sizes. The half-width is defined as the transverse difference between the y-positions where the mean axial velocity is equal to the average of the centerline velocity and the free stream velocity

$$y_{1/2} = y \left(\frac{u_{cl} + u_{\infty}}{2} \right) \Big|_{top} - y \left(\frac{u_{cl} + u_{\infty}}{2} \right) \Big|_{bottom}$$
(3.1)

The findings confirm the existence of "ghost particles", which were hypothesized by Ferrante and Elghobashi (2003). From the plot, it is clear that the larger particles damp the Kelvin-Helmholtz instabilities which, in turn, decrease the growth rate of the jet; yet it is also apparent that the addition of tiny particles slightly amplifies the instabilities leading to a small increase in the growth rate. Therefore, it seems entirely probable that there is a particular particle size that will have a minimal effect on the turbulence. A poignant finding is that the particle with $\tau_p = 1.0$ have the largest damping effect on the carrier gas. Physically this could be explained as particles that have a particle response time that is on the order of the time scale of the carrier gas turbulent kinetic energy (TKE) will tend to dissipate the TKE in a way similar to added viscous effects, damping the instabilities. The non-linearity of the correlations for particle drag makes it very

difficult to correctly analyze (or verify) the effect of particle inertia on turbulence directly from theory.

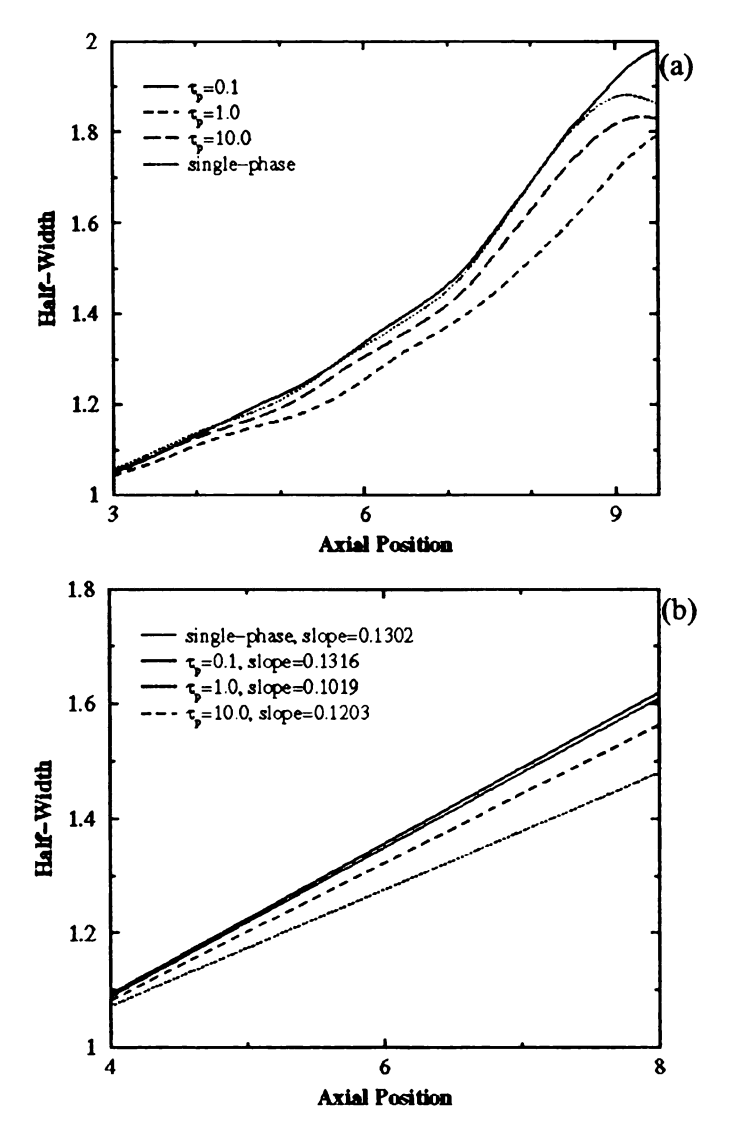


Figure 6. Effect of particle time constant on jet growth rate. (a) whole field and (b) regression analysis of "self-preserving" region

Figure 7 shows the instantaneous values of the particle centerline axial velocity for various τ_p . Note the similarity between the cases with $\tau_p = 0.1$ and $\tau_p = 1.0$. The difference in peaks of these two cases indicates that the larger particles are not accelerated up to the fluid's local velocity, but rather have a finite drag. It is important to

emphasize that the plot represents the instantaneous velocity, not the mean (time-averaged or ensemble).

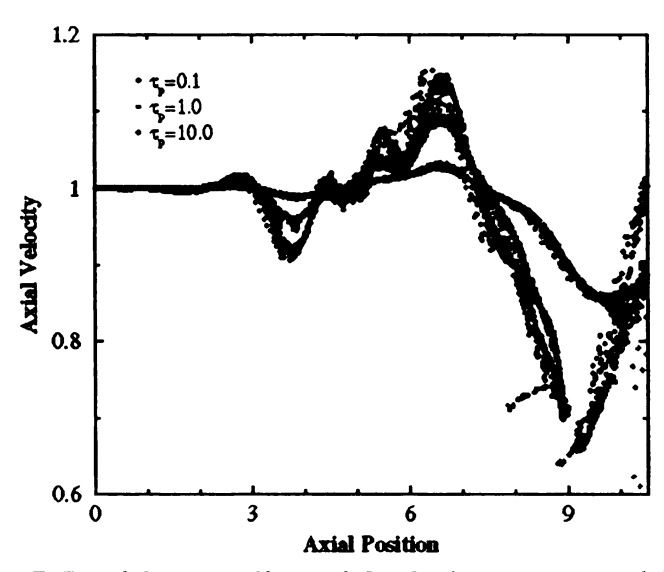


Figure 7. Particle centerline axial velocity versus particle size

Figure 8 shows that an increase in mass-loading will amplify the effect of the particles on the carrier gas as expected. There is a significant decrease in the slope of the linear region as the mass-loading ratio is increased. This decrease follows a linear trend. Using the mass loading as the independent variable (x) and the slope of the half-width in the self-similar region as the dependent variable (y), a linear regression analysis shows that y = -0.1051x + 0.1284, r = -0.9891; verifying the linear nature of the effects of mass-loading on jet growth rate. Although not investigated directly, it would seem that if the particles were small, they would increase the growth rate (as discussed previously). This increase would be amplified by increasing the mass-loading ratio just as the growth rate is attenuated by the addition of more large particles.

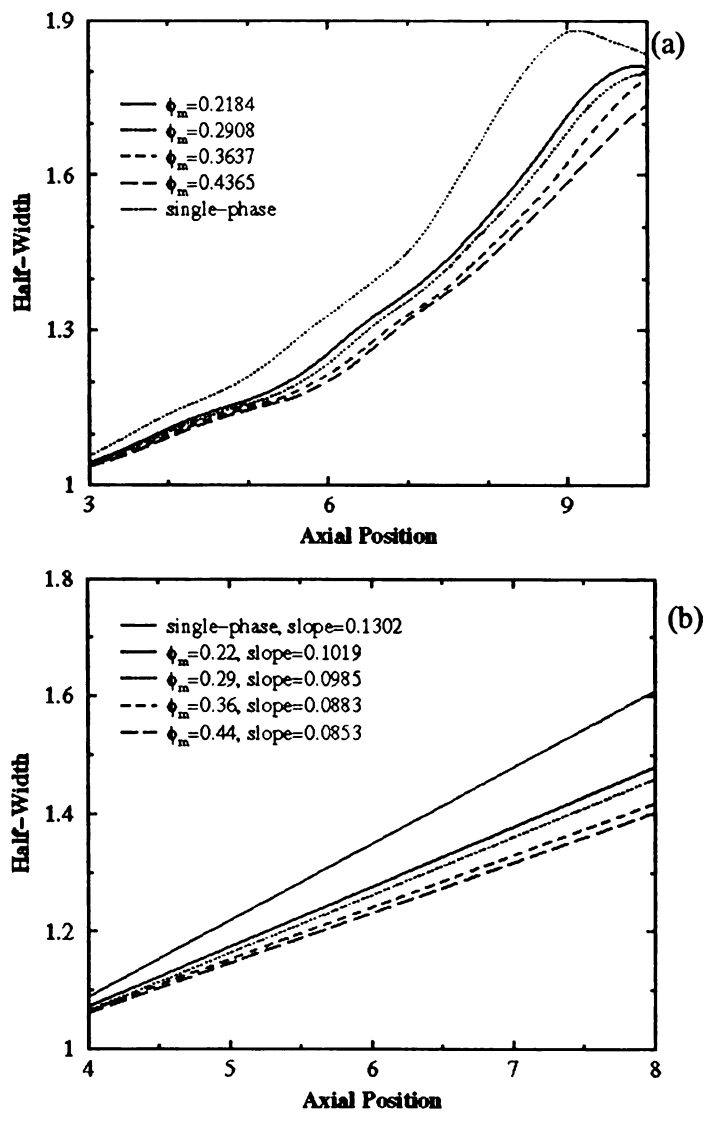


Figure 8. Effect of mass-loading on jet growth rate. (a) whole-field and (b) regression analysis of self-preserving region

These effects can also be seen by looking at the axial velocity profiles. The centerline mean axial velocity of single-phase free jets decays as $x^{-1/2}$ in the self-similar region. This decay rate is expected to be lowered by the addition of large particles. Figure 9 shows the centerline axial velocity profiles. Note the decrease in jet mean velocity decay as the mass-loading ratio is increased. The root-mean-square (RMS) of axial velocity trend is altered in a similar way. The RMS value reaches a higher peak earlier in the flow with

lower mass-loading. Then it decays faster than the higher mass-loading cases. There is a 'cross-over' point around x/h = 9.

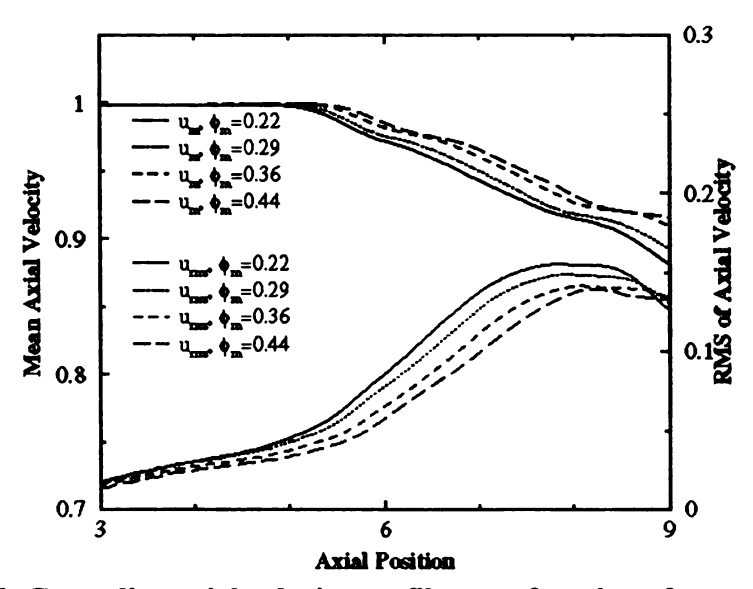


Figure 9. Centerline axial velocity profiles as a function of mass-loading

Another important variable to consider when investigating planar jets is the Reynolds

stress term, $\overline{u'v'}$, that appears in the production part of the TKE equation. For convenience, the Reynold's stress and the Production of TKE are averaged over the length normal to the direction of interest. For example, the plot of $\overline{u'v'}$ versus x is actually the plot of $\frac{1}{2 \cdot y_{\text{max}}} \int \overline{u'v'} dy$ versus x. Figure 10 shows the axial and transverse variations of the Reynolds stress as functions of mass-loading. The Reynolds stress peak magnitude is nearly halved with the addition of particles at a mass-loading ratio of 0.44, and the integral of the velocity correlation term in the transverse direction is clearly less than half of the single-phase case. When particles are added to the flow, the growth of the Reynolds stress along the shear layer is severely hampered, indicating an increase in the stability of the jet.

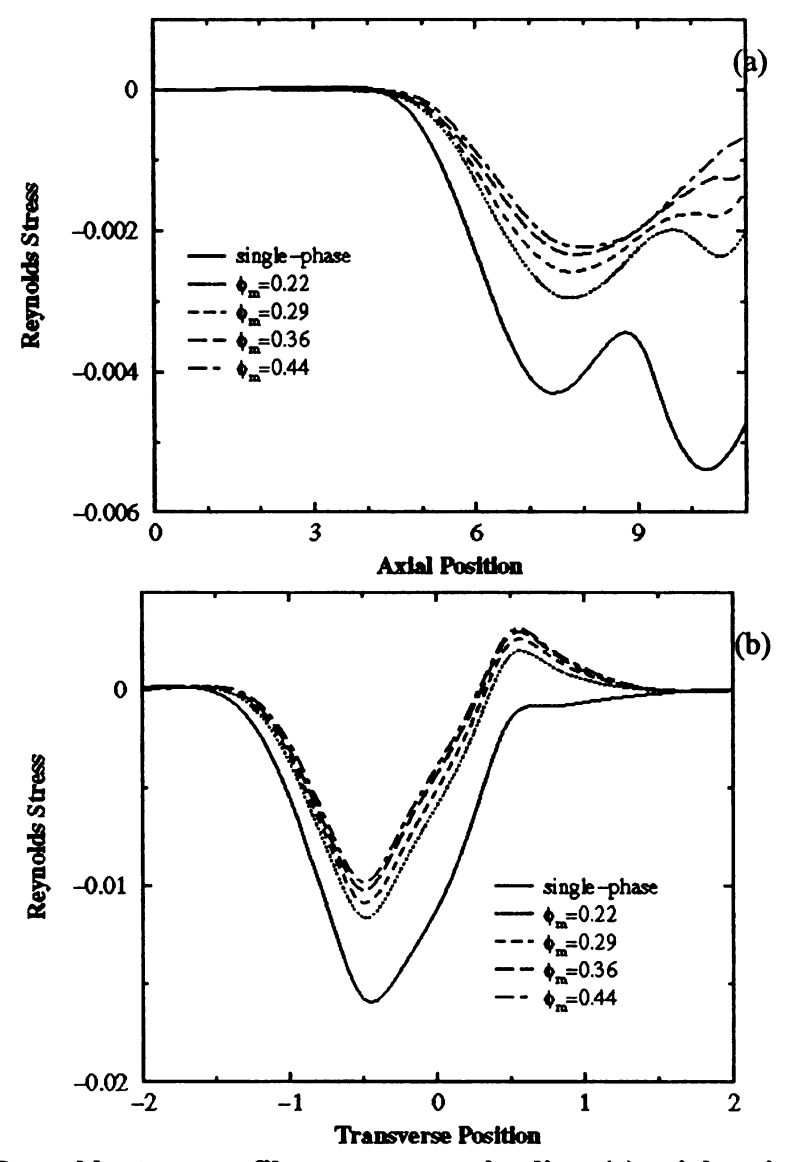


Figure 10. Reynolds stress profiles versus mass-loading. (a) axial variation at the shear layer and (b) transverse variation at x/h=6

It is also easy to see the effects of the mass loading on the turbulence by considering the production term (of the TKE equation) as a whole. The inclusion of the mean velocity gradient helps to see the net production effects, not just the Reynolds stress. Figure 11 shows the production profiles for different mass loading ratios. The most significant observation is that the production of TKE on the positive y-half of the jet swaps from negative to positive when moderately-sized particles are added to the flow. This shift

from somewhat antisymmetric to symmetric production of TKE causes a change in the jet development mechanism. There is also a noticeable difference in the magnitude of production of TKE in the axial direction downstream of the jet inlet. The shear layer is where the production should be close to its maximum. The cases with particles clearly show a significant deviation from the results for single-phase flow.

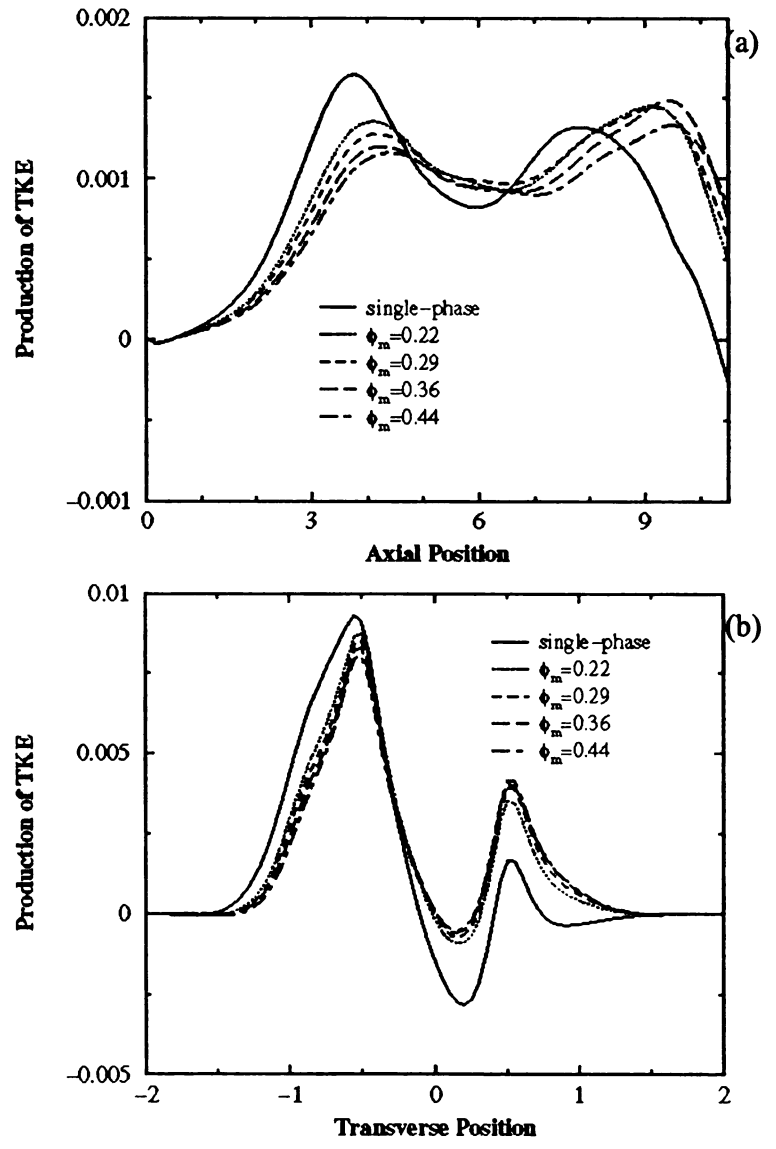


Figure 11. Production of TKE profiles versus mass loading. (a) axial variation at the shear layer and (b) transverse variation at x/h = 6

The temperature effects for the two-way coupling cases 7 and 8 without evaporation show interesting aspects of the particles' thermal inertia. The non-physical case (Case 7), for which the thermal interactions between particles and carrier gas is not allowed and the particle temperature is artificially held constant, aids in the understanding of the additional density effects due to the temperature difference. The more physical case (Case 8) involves much more complicated particle-gas interactions. For one, the particles act as temperature sinks, dropping the carrier gas temperature in the core of the flow. This causes a density stratification wherein the high-speed flow is cooler (and thus higher density) than the low speed flow. This acts to stabilize the jet, decreasing the growth rate (Colucci (1994)). It also causes the entrainment velocity to increase. The centerline mean axial velocity profiles of Cases 2, 7 and 8 are shown in Figure 12, and the variation of the mean axial velocity profiles are shown in Figure 13. When the gas temperature is increased but the particles are not allowed to have thermal interaction, the mean axial velocity is nearly unchanged, while the RMS of axial velocity is significantly damped, especially in the region where the particles are more highly concentrated. When the particles are allowed thermal interaction with the carrier gas, the centerline mean axial velocity is attenuated, while the RMS of axial velocity is nearly unchanged. This would seem to imply that the instabilities generated by the particles are nearly balanced by the attenuation of the instabilities due to temperature differences.

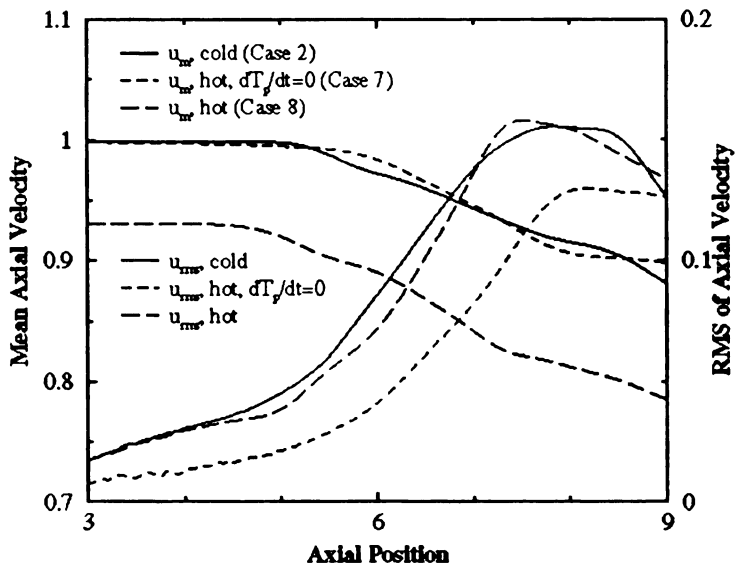


Figure 12. Temperature effects for two-way coupling cases at jet centerline

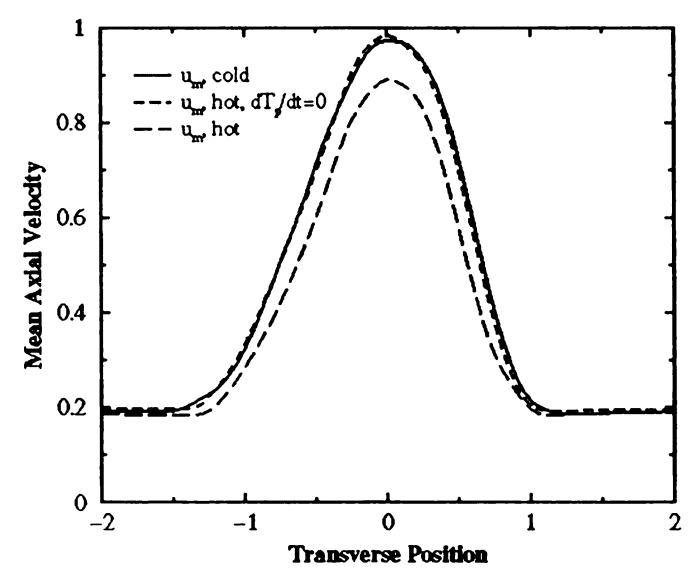


Figure 13. Two-way coupling temperature effects on velocity profiles at x/h=6

2.2.2 Evaporating Droplets

There are several interesting effects that evaporation has on the gas-droplet interaction in a planar jet. These are best analyzed by isolating the evaporative effects from the momentum and heat interactions that are discussed above for the non-evaporative cases. Table 3 explains the different cases relevant to evaporation, Figure 14 shows the growth

rate of the jet half-width for the different cases, and Figure 15 shows the centerline velocity trends for the same cases. A special case was considered to discern the flow modification due to density stratification and due to phase interactions. A case without particles was conducted wherein the initial temperature profile was chosen to approximate the profile observed in the evaporating cases. The temperature of the jet was reduced from nondimensional temperature T=2.04 to T=1.5; the co-flow was kept at T=2.04. In Figure 14(b), the jet development is quantified by calculating the approximate slope of the jet half-width at different locations from the jet nozzle. This plot shows that the addition of particles with no temperature or mass interaction does not significantly change the jet growth rate. When the temperature effects of the particles are considered, there is a very large change in the growth rate. When there are no particles and the initial non-uniform jet density profile is introduced, the modification to the jet growth is slightly less than the thermally coupled case. Also, when the effects of evaporation are considered, the jet growth rate is damped as compared to the two-way coupled case with no evaporation. The density stratification effects seem to contribute significantly, but not exclusively to the modification of the jet growth rate.

Table 3. Evaporative case descriptions

Case	Description		
Case 1	Single-phase/One-way		
Case 2	One-way with Density Stratification		
Case 3	Two-way, with $dT_p/dt = 0$		
Case 4	Two-way		
Case 5	Evaporation		

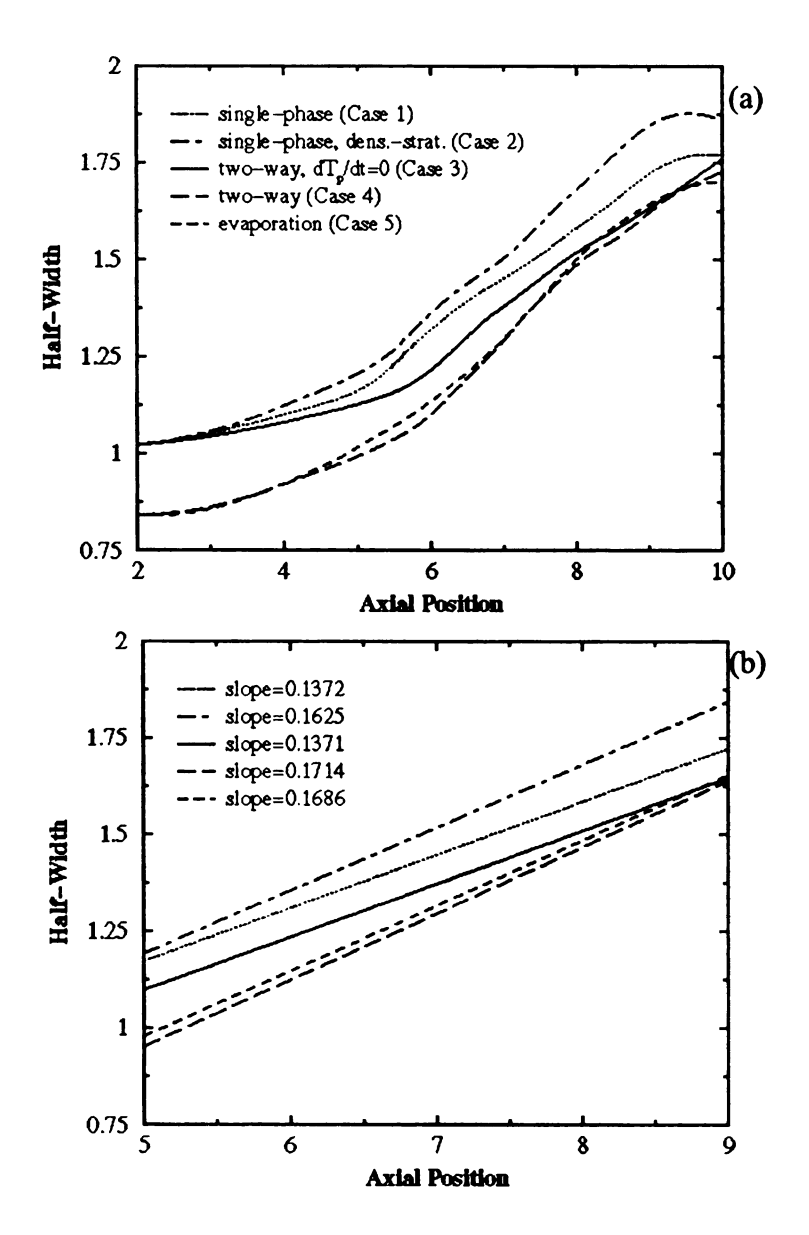


Figure 14. Jet half-width versus coupling (T=600) (a) actual growth, and (b) linear regression of the linear portion of the growth rate

What is striking in Figure 15 is the modification of the RMS of axial velocity. The difference between the two-way coupling cases with and without evaporation seems to be more pronounced in the velocity fluctuations. The tendency of the RMS of axial velocity to decay rapidly after reaching its peak is reduced in the evaporative case. It would seem

as though the added mass due to evaporation damps the peak value, but sustains the turbulence levels further beyond that peak.

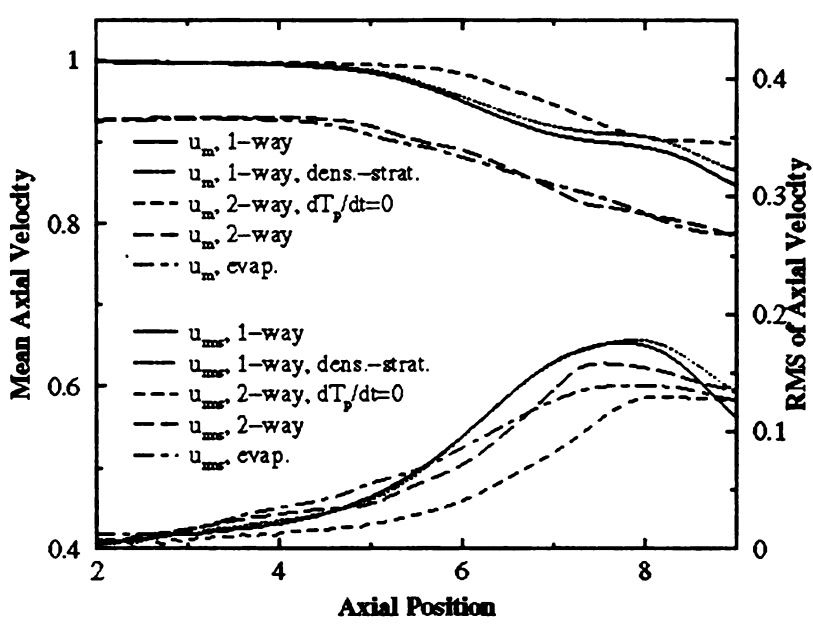


Figure 15. Centerline axial velocity profiles as a function of coupling (T=600)

The Reynolds stress profiles for the different one- and two-way coupling cases are shown in Figure 16. Note the considerable modifications in production due to the evaporative effects. Specifically, there is a considerable decrease in the Reynolds stress at the shear layer for the two-way coupled case. The case with evaporation showed an increase in Reynolds stress over the two-way coupled case except between $x/h \approx 7$ and 9. A decrease in the Reynolds stress is generally associated with a decrease in the velocity fluctuations, effectively increasing the stability of the jet. Hence, a decrease in the growth rate of the jet is to be expected.

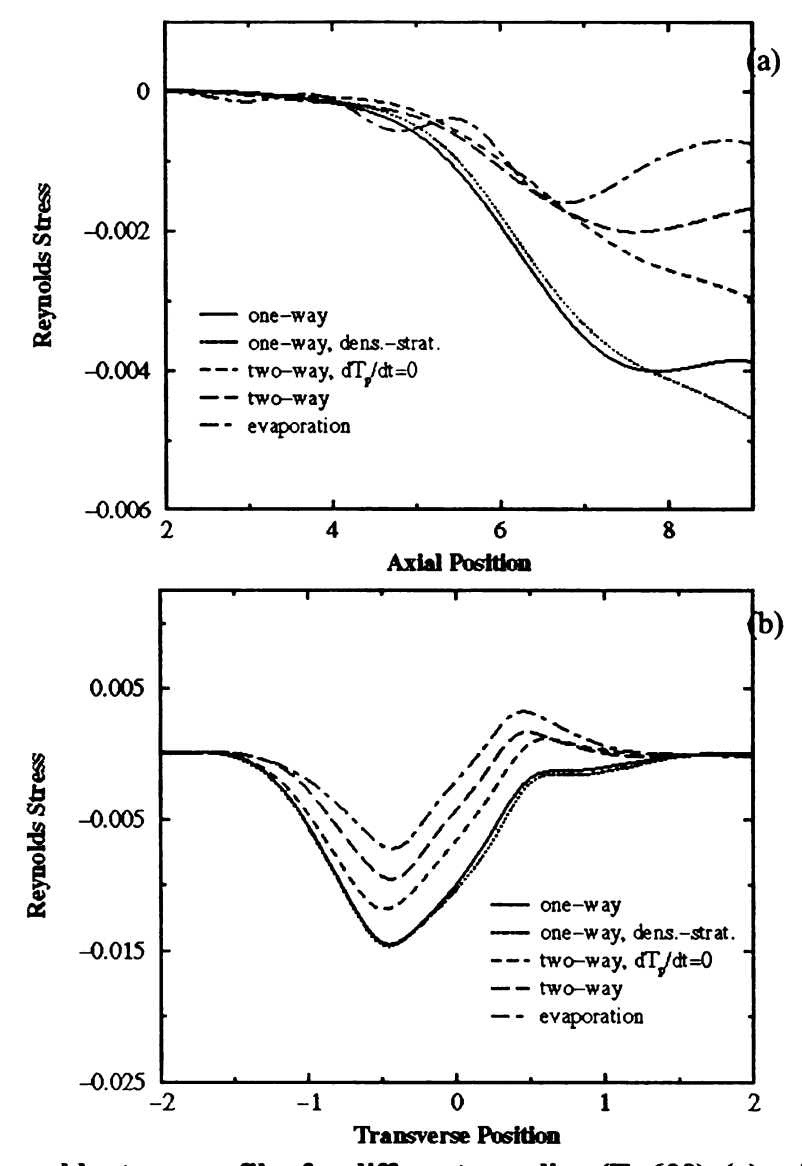


Figure 16. Reynolds stress profiles for different coupling (T=600). (a) axial variation at shear layer and (b) transverse variation at x/h=6

The modification of TKE production due to evaporative effects can be seen in Figure 17. Of particular interest is the increase in the peak of the production of TKE from the non-evaporating to the evaporating case near $x/h \approx 9$, as seen in Figure 17(a). Farther downstream, the two curves tend toward each other. There is also a definite increase in the production of TKE in the evaporation case over the one-way case with density

stratification. Evidently, the density-stratification has increased production initially, followed by a steady decline towards the one-way coupled case with uniform density.

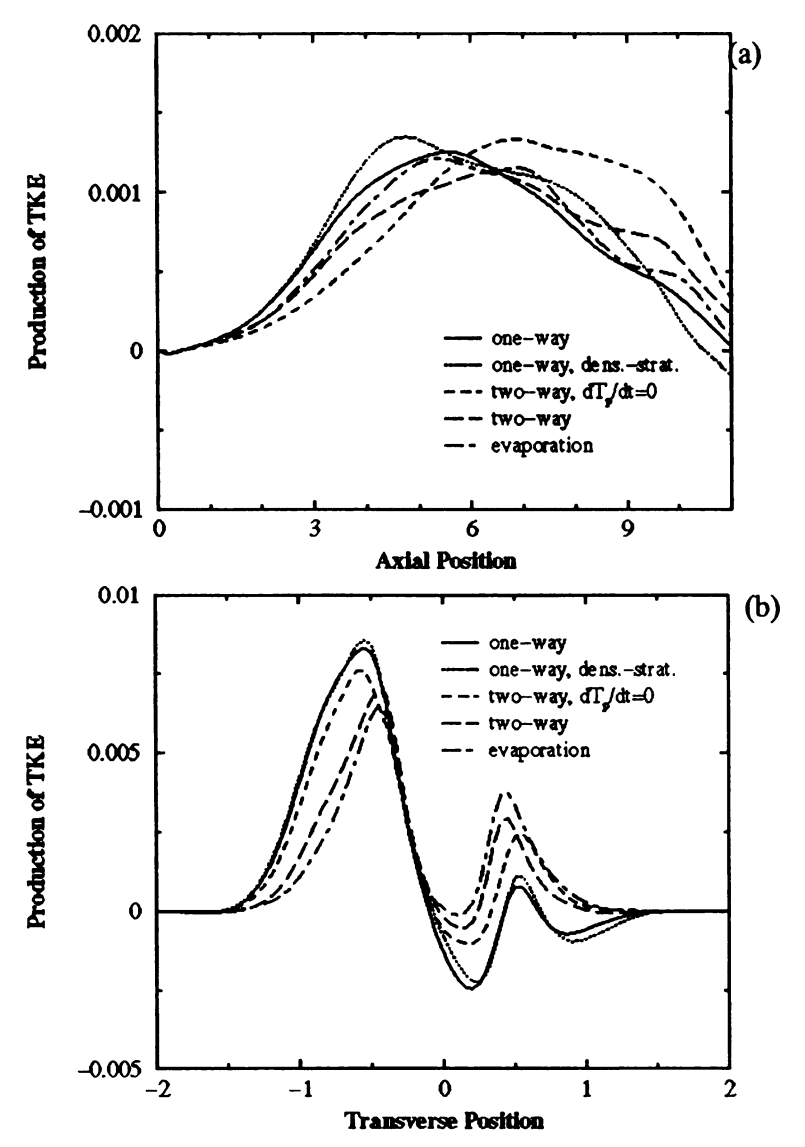


Figure 17. Production of TKE profiles for different coupling (T=600). (a) axial variation at the shear layer and (b) transverse variation at x/h = 6

It is important to realize that the effects of evaporation are attributed to several competing physical occurrences. The non-evaporative particles in the hot environment will act as temperature sinks, but the addition of evaporation will decrease the temperature even

more. The axial temperature profiles for evaporating and non-evaporating cases are shown in Figure 18, which clearly shows a nearly constant decrease in temperature downstream of the jet inlet. The value of this decrease is about 0.2 non-dimensional temperature units, or approximately 55K in standard units, give the parameters used for this study. The one-way density-stratified case seems to agree more favorably with the two-way coupled case than the evaporative case, indicating that the added mass effects in the evaporative case uniquely modify the jet.

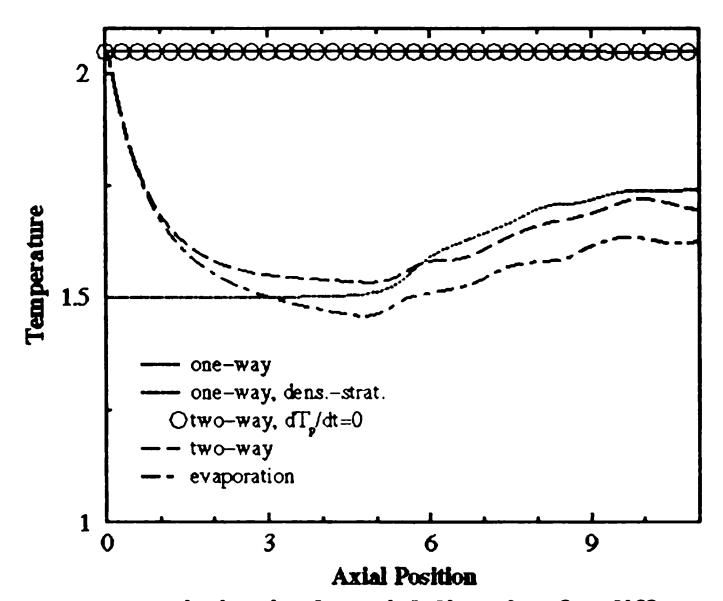


Figure 18. Temperature variation in the axial direction for different coupling cases.

In addition to its effects on temperature, the evaporate vapor will contribute mass, adding to the density of the carrier gas. These combined effects may explain the observed differences between the cases with and without evaporation considered. The density and mass fraction of vapor variation due to temperature and evaporate added mass effects are shown in Figure 19. It is important to note that the nondimensionalization of the variables leads to the ability to directly add or subtract the density and the mass fractions. The difference in density between the two-way coupled cases with and without evaporation is

nearly mimicked by the mass fraction of evaporate plot. There is, however, a small difference between these two that is due to the actual heat of vaporization of the droplets modifying the temperature and density fields.

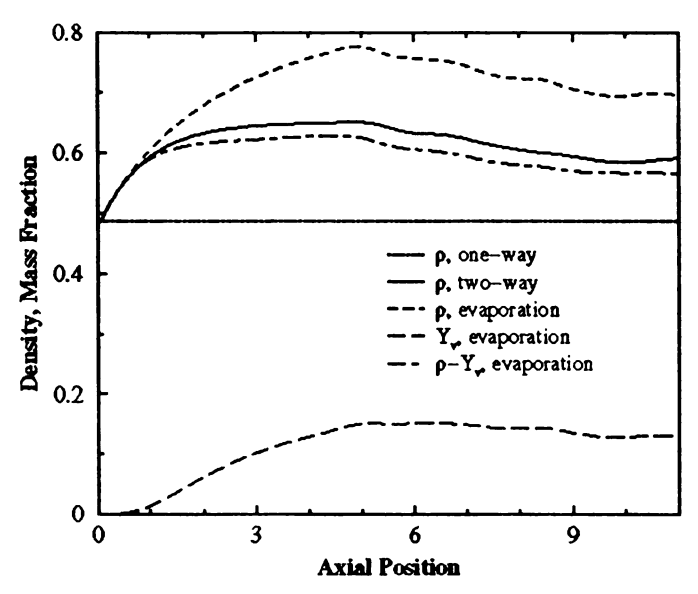


Figure 19. Density and mass fraction of vapor variation in the axial direction for different one- and two-way coupling cases

The transverse variation of temperature and density are shown in Figure 20. Not the clear density stratification due to the temperature and added mass effects. The effects of density stratification are explained in the introduction section and throughout this paper. To summarize, if the higher speed stream is of lower density than the lower speed stream, the Kelvin-Helmholtz instabilities will be attenuated. Add to that the effects of the particle drag, etc. and there are interesting modifications to the jet structure.

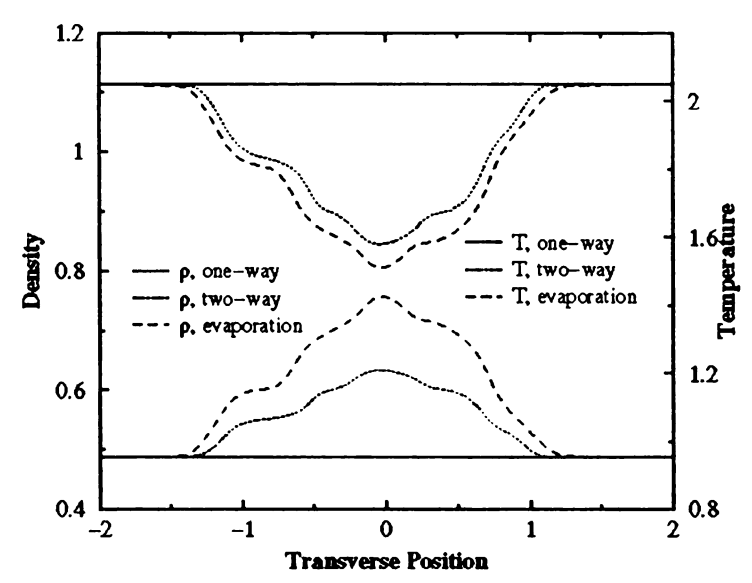


Figure 20. Transverse variation of temperature and density

As discussed previously, different sizes of droplets or particles have different effects on the carrier gas (and the carrier gas affects them differently as well). Clearly, if droplets evaporate at different rates, there will then be a size distribution that could cause interesting modifications to the statistical properties of the turbulence. A plot of the development of the probability distribution function (pdf) of particle mass for the $\tau_p = 1.0$ case is shown in Figure 21. The pdf of particle mass at the inlet would look like a delta function, as the injection parameter was set to uniform particle size. As the flow develops and droplets begin to evaporate, the pdf shifts towards a more Gaussian shape, indicating that there are some particles that are not evaporating very much and that some are vaporizing very rapidly. The plot does not allow for the discernment of local vaporization rates, as it represents the pdfs of all of the particles at a particular x-location (integrated over y). Figure 22 show a comparison of the local average particle mass and the Reynolds stress. The transverse profiles show that at locations where the droplets have evaporated (i.e. small droplets), there is an increase in the Reynolds stress. This seems to correlate

well with the notion that smaller particles enhance the TKE, while larger particles attenuate the turbulence.

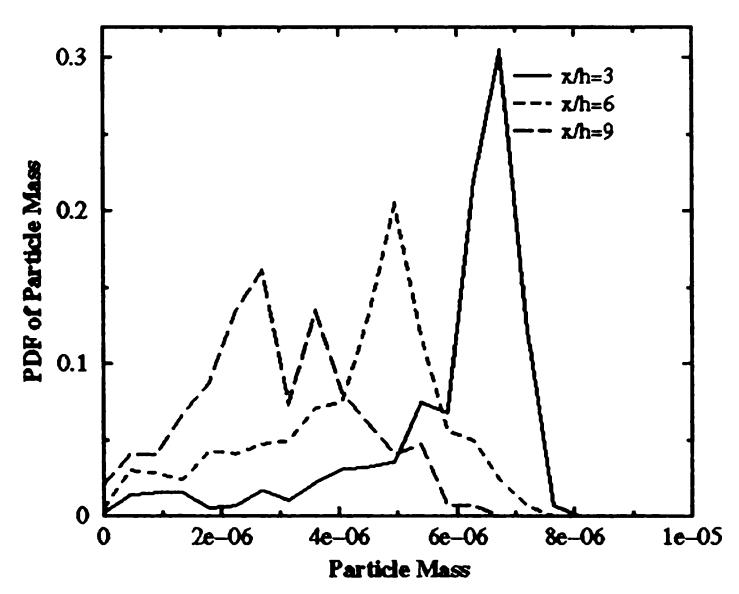


Figure 21. Development of the probability distribution function of particle mass

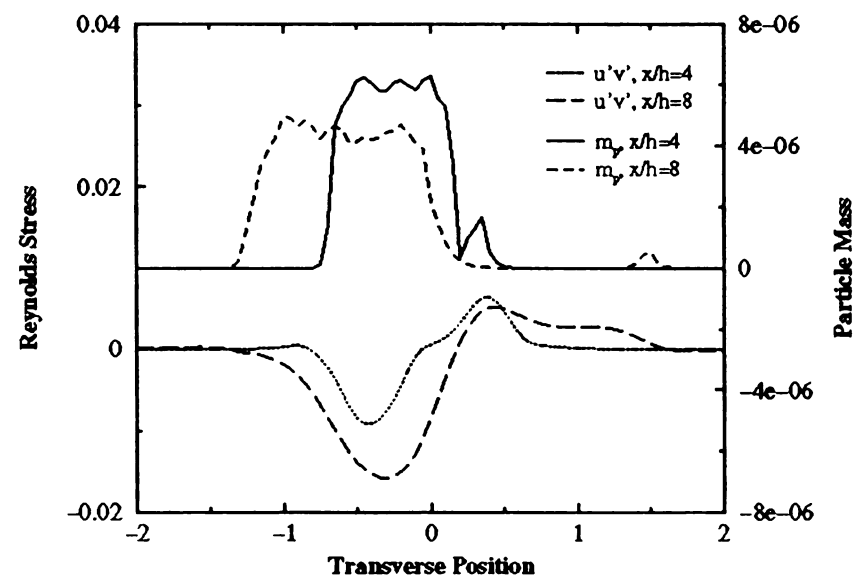


Figure 22. Eulerian averaged particle mass and Reynolds stress profiles at various downstream locations

2.2.3 Interpolation

To verify the accuracy of the numerical schemes used in this study, various tests were devised and implemented. One of the more crucial aspects of the Eulerian-Lagrangian formulation requires the accurate calculation of the carrier gas properties at the particle or droplet location, which requires interpolation. Two different interpolation schemes were implemented for this work: first-order linear and fourth-order Lagrange polynomial. The results for the two cases were compared, and the accuracy of the linear interpolation was determined to be sufficient to resolve the physics of the jet. This was indeed fortuitous, as the computational efficiency of the linear scheme was nearly twice that of the Lagrangian scheme. The case used for comparison was the most complicated physically, including evaporative effects at high temperatures. Figure 23 shows the temperature profiles of the two interpolation schemes, and Figure 24 shows the jet half-width growth rate.

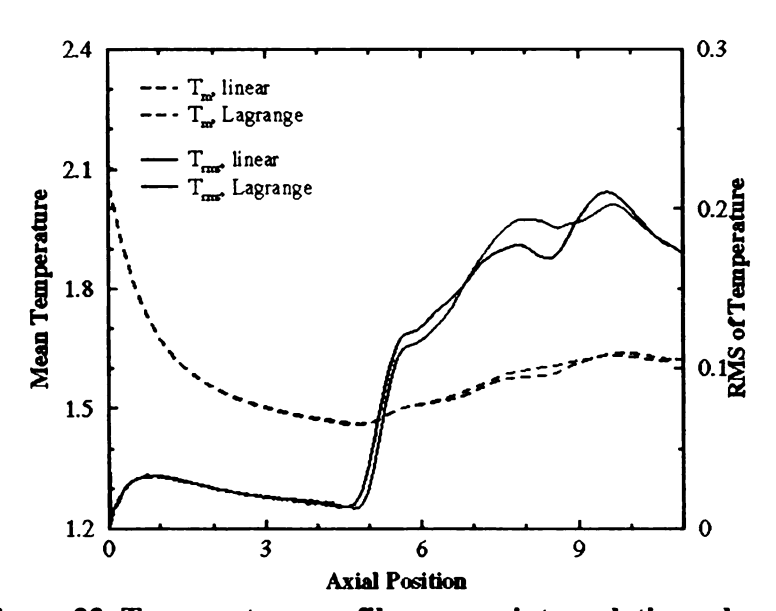


Figure 23. Temperature profiles versus interpolation schemes

While there are some differences to be noted, the two are within any acceptable experimental margin of accuracy. It is important to realize that some of the larger

variations at near the outlet could be attributed to numerical growth of physical inaccuracies that are commonly associated with certain boundary conditions.

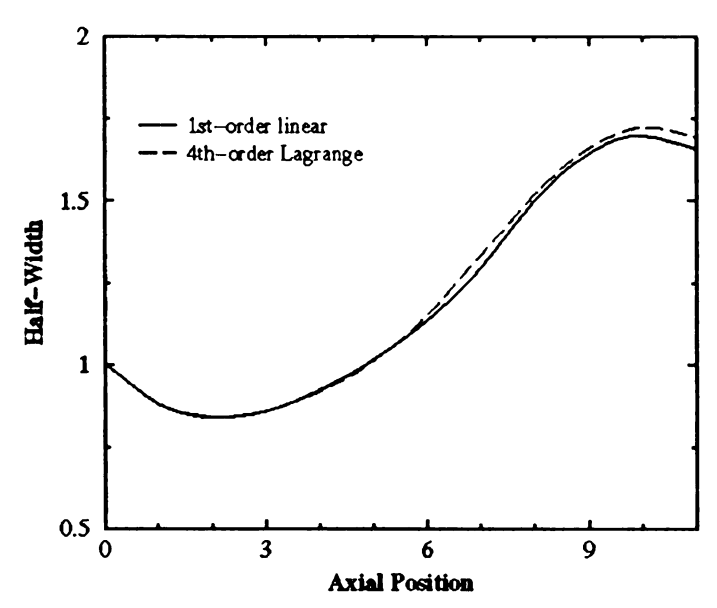


Figure 24. Jet growth rate as a function of interpolation scheme

CHAPTER 3 LARGE-EDDY SIMULATIONS OF A ROUND JET

3.1 Governing equations and computational methodology

In large eddy simulation (LES) methods, the "resolved" carrier gas field is obtained by solving the filtered form of the compressible continuity, Navier-Stokes, energy and scalar equations, together with the equation of state for pressure

$$\frac{\partial \langle \rho \rangle}{\partial t} + \frac{\partial \langle \rho \rangle_l \langle u_i \rangle_L}{\partial x_i} = \left\langle S_\rho \right\rangle_l \tag{3.1}$$

$$\frac{\partial \langle \rho \rangle_{l} \langle u_{i} \rangle_{L}}{\partial t} + \frac{\partial \langle \rho \rangle_{l} \langle u_{i} \rangle_{L} \langle u_{j} \rangle_{L}}{\partial x_{j}} = -\frac{\partial \langle p \rangle_{l}}{\partial x_{i}} + \frac{1}{\text{Re}} \frac{\partial \langle \tau_{ij} \rangle_{l}}{\partial x_{j}}$$

$$-\frac{1}{\text{Re}}\frac{\partial \langle \Gamma_{ij} \rangle_l}{\partial x_i} + \langle S_{ui} \rangle_l \tag{3.2}$$

$$\frac{\partial \langle \rho \rangle_l \langle E \rangle_L}{\partial t} + \frac{\partial \langle \rho \rangle_l \langle u_i \rangle_L \langle E \rangle_L}{\partial x_i} = -\frac{1}{(\gamma - 1)Ma^2 \operatorname{RePr}} \frac{\partial \langle q_i \rangle_l}{\partial x_i} - \frac{\partial N_i}{\partial x_i}$$

$$+\langle \rho S_e \rangle_l$$
 (3.3)

$$\frac{\partial \langle \rho \rangle_{l} \langle Y_{\alpha} \rangle_{L}}{\partial t} + \frac{\partial \langle \rho \rangle_{l} \langle u_{i} \rangle_{L} \langle Y_{\alpha} \rangle_{L}}{\partial x_{i}} = -\frac{1}{\text{Re Pr } Le_{\alpha}} \frac{\partial \langle J_{i}^{\alpha} \rangle_{l}}{\partial x_{i}} - \frac{\partial M_{i}^{\alpha}}{\partial x_{i}}$$

$$+\left\langle \rho S_{\alpha}\right\rangle_{l} + \left\langle S_{\rho}^{\alpha}\right\rangle_{l}, \alpha = 1, 2, ..., N_{s}$$
(3.4)

$$\langle p \rangle_l \approx \langle \rho \rangle_l R^0 \langle T \rangle_l \sum_{1}^{N_s} \frac{\langle Y_\alpha \rangle_L}{W_\alpha}$$
 (3.5)

$$\langle \tau_{ij} \rangle \approx \langle \mu \rangle_L \left(\frac{\partial \langle u_i \rangle_L}{\partial x_j} + \frac{\partial \langle u_j \rangle_L}{\partial x_i} - \frac{2}{3} \delta_{ij} \frac{\partial \langle u_k \rangle_L}{\partial x_k} \right), \langle \mu \rangle_L = \Pr \langle k / C_p \rangle_L$$
 (3.6)

where $\langle f(\mathbf{x},t)\rangle_I$ and $\langle f(\mathbf{x},t)\rangle_L = \langle \rho f \rangle_I/\langle \rho \rangle_I$ represent the filtered and the Favre-filtered values of the transport variable $f(\mathbf{x},t)$ and ρ , u_i , p, T, E, and Y_α are the fluid density, velocity, pressure, temperature, energy and mass fraction of species α , respectively. In equation (3.5) μ , k, C_p and Pr are the viscosity coefficient, the thermal conductivity coefficient, the specific heat and the Prandtl number, respectively. R^0 denotes the universal gas constant and W_α is the molecular weight of species α . The subgrid-scale (SGS) closures that appear in the above filtered equations include the SGS stress $\langle \Gamma_{ij} \rangle = \langle \rho \rangle_L \left\langle u_i u_j \right\rangle_L - \langle u_i \rangle_L \left\langle u_j \right\rangle_L \right|$ and the SGS energy and scalar fluxes. Jaberi and Colucci (2003) describe the SGS models chosen for this particular body of work in detail. Here all of these terms are modeled with "standard" diffusivity closures. The effects of the droplets on the carrier fluid are expressed through the mass (S_ρ) , momentum (S_{ui}) and energy (S_e) source/sink terms as described below.

The droplet field is solved via a Lagrangian method under the point-source approximation. In this method, the evolution of the droplet displacement vector (X_i) , the droplet velocity vector (v_i) , the droplet temperature (T_p) , and the droplet mass (m_p) , is governed by the following equations

$$\frac{dX_i}{dt} = v_i \tag{3.7}$$

$$\frac{dv_i}{dt} = \frac{f_1}{\tau_p} \left(u_i^* - v_i \right) \tag{3.8}$$

$$\frac{dT_p}{dt} = \frac{\eta f_2}{\tau_p} \left(T^* - T_p \right) + \frac{L_v}{m_p c_L} \frac{dm_p}{dt}$$
(3.9)

$$\frac{dm_p}{dt} = -\frac{m_p f_3}{\tau_p} \ln(1 + B_M) \tag{3.10}$$

where the asterisk refers to the local fluid variables, which are interpolated to the droplet position, and τ_p is the normalized droplet time constant. The variables η , f_1 , f_2 and f_3 are functions of the droplet and carrier gas parameters such as the droplet drag coefficient, the droplet Reynolds number, and the Prandtl number. B_M is the mass transfer number as calculated by the Langmuir-Knudsen non-equilibrium model. In the following terms

$$\eta = \frac{\beta}{e^{\beta} - 1}, \quad \beta = -\left(\frac{3 \operatorname{Pr} \tau_p}{2}\right) \frac{1}{m_p} \frac{dm_p}{dt}$$
(3.11)

$$f_1 = \frac{C_D \operatorname{Re}_p}{24} \tag{3.12}$$

$$f_2 = \frac{Nu}{3 \operatorname{Pr} \alpha}, \quad \alpha = \frac{C_l}{C_p} \tag{3.13}$$

$$f_3 = \frac{Sh}{3Sc} \tag{3.14}$$

where Re_p is the Reynolds number based on the particle diameter and the slip velocity, Re_b is the blowing Reynolds number due to evaporative blowing velocity, Nu is the Nusselt number, Sh is the Sherwood number and Sc is the Schmidt number.

The volumetric source terms appearing in the carrier gas equations are evaluated based on the volumetric averaging of the Lagrangian field as

$$S_{\rho} = -\frac{1}{\delta V} \sum \left\{ -m_p \left[\frac{f_3}{\tau_p} \ln(1 + B_M) \right] \right\}$$
 (3.15)

$$S_{ui} = -\frac{1}{\delta V} \sum \left\{ m_p \frac{f_1}{\tau_p} (u_i^* - v_i) + \frac{m_p v_{dri}}{\tau_p} - m_p \left[\frac{f_3}{\tau_p} \ln(1 + B_M) v_i \right] \right\}$$
(3.16)

$$S_e = -\frac{1}{\delta V} \sum \left\{ \frac{C_p \alpha}{(\gamma - 1) Ma^2} m_p \left[\frac{\eta f_2}{\tau_p} \left(T^* - T_p \right) + \frac{f_1}{\tau_p} \left(u_i^* - v_i \right) v_i + \frac{v_{dri} v_i}{\tau_p} \right] \right\}$$

$$-m_{p}\left[\frac{f_{3}}{\tau_{p}}\ln(1+B_{M})\right]\left[\frac{h_{v,s}}{(\gamma-1)Ma^{2}}+\frac{v_{i}v_{i}}{2}\right]$$
(3.17)

where the summation is taken over all droplets in the volume $\delta V = \delta x^3$ centered at each Eulerian (grid) point. Equations (3.1)-(3.17) describe the general Eulerian-Lagrangian formulation of a compressible two-phase turbulent system with full mass, momentum and energy coupling between carrier and dispersed phases. For the purposes of this study, the effects of gravity and evaporation are ignored. Hence, g_i , v_{dri} , \dot{m}_p and S_ρ are zero.

In LES, the above filtered carrier-gas equations are solved together with diffusivity-type closures for the SGS stress and the SGS energy flux terms. For the droplet phase, a stochastic model is considered in which the SGS diffusivity (evaluated from large scale quantities) is used to construct the residual or subgrid velocity of the carrier fluid at the droplet location. The combined large- and small-scale fluid velocity is used to move the droplets and to calculate the droplet drag force. The discretization procedure of the carrier fluid is based on the "compact parameter" finite difference scheme, which yields up to sixth order spatial accuracies. The time differencing is based on a second order method. Once the fluid velocity, density and temperature fields are known, the droplet transport

equations are integrated via the second order Adams-Bashforth scheme. The evaluation of the fluid properties at the droplet locations is based upon a second and fourth order accurate Lagrangian interpolation scheme. The location and size of droplets at the jet inlet vary in different simulations.

3.2 Results and discussion

3.2.1 Comparison with experiment

An a posteriori analysis is conducted to assess an stochastic subgrid-scale (SGS) closure used in the large-eddy simulation (LES) method for computing two-phase turbulent flows. Specifically, LES and experimental results for a particle-laden axisymmetric turbulent jet are compared. The experimental results are taken from U. Fritsching, et al. (2001), for which a phase-Doppler anemometry (PDA) system is used to measure the velocities of the seeded carrier gas and particles. The physical parameters for the two-phase flow configuration are given in Table 4. An analysis of the results for the single-phase flow configuration is also included, although an emphasis is placed on the ability of LES to accurately represent multiphase effects. A qualitative picture of the flow configuration is shown in Figure 25.

Table 4. Physical parameters

Table to Lajoleta parameter			
Reynolds number	5700		
Tube diameter	12mm		
Carrier gas	Air		
Mean particle diameter	110μm		
Mass loading	1		
Dispersed phase	Glass beads		

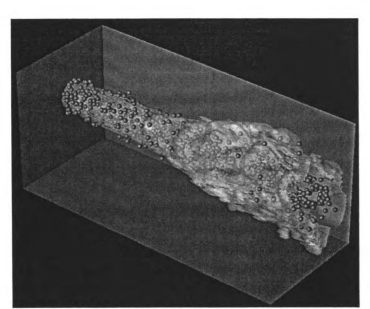


Figure 25. Vorticity magnitude and particle distribution

The data for three different LES cases are compared to the experimental results: Case 1) no SGS model for particle-carrier gas interaction with uniform inlet particle size distribution; Case 2) an stochastic SGS model for particle dispersion with uniform particle size distribution; and Case 3) an stochastic SGS model with Gaussian particle size distribution. A summary of these cases is given in Table 5. Three variables in particular are used to compare the results: mean axial velocity, u_m, root-mean square (RMS) of axial velocity, u_{ms}, and turbulence intensity, Tu. These variables are measured/calculated at various locations in the flow field. The results are reported for single- and two-phase flows, and for LES with various SGS closure/particle size configurations.

Table 5. Case summary

Case	SGS Particle Model	Particle Size Distribution	
1	No	Uniform	
2	Yes	Uniform	
3	Yes	Gaussian	

A plot of centerline mean axial velocity versus downstream location for the experimental and computational results of two-phase cases is shown in Figure 26. Note that Case 3, the case with SGS particle closure and initial Gaussian particle size distribution, best reproduces the experimental centerline velocity. Case 2 is nearly as accurate as Case 3 and Case 1 is considerably inaccurate in comparison to the other cases. This is the first indication that the new SGS closures are indeed viable. The slight increase in accuracy from Case 2 to Case 3 indicates that some of the errors associated with the LES calculations are due to actual physical variations in inlet particle size and locations, and are not simply due to modeling errors. The difference between experimental and numerical results is better shown in Table 6, where the percent error for centerline mean axial velocity at several axial locations is considered.

Figure 27 shows the radial variation of axial velocity at two different axial locations and Table 7 gives some sample percent error calculations for those locations. Note that the difference between LES and experimental results at x/D = 7.5 increases with increasing radius (i.e., the tails match less), but that farther downstream (at x/D = 12.5), they match much better. The percent error calculations show that there are positions where each case best matches the experimental data. However, on average, the results of Case 3 are significantly better than the other two.

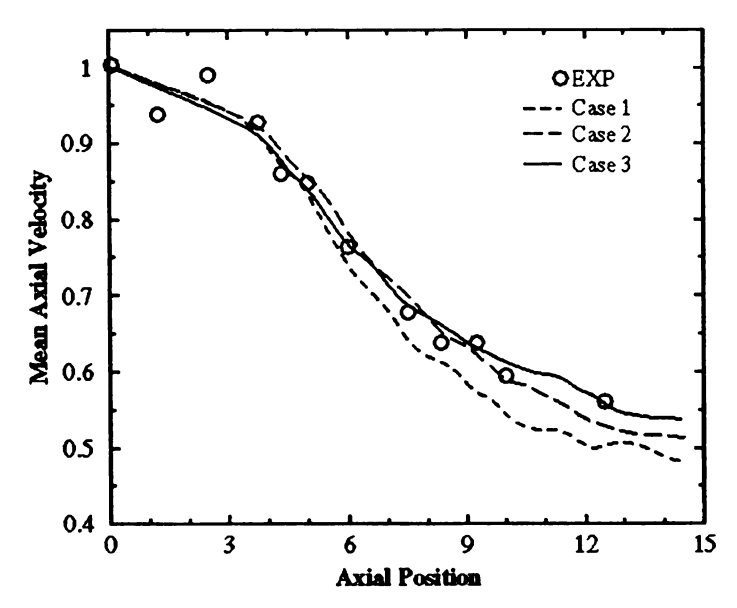


Figure 26. Centerline mean axial velocity versus downstream location

Table 6. Sample percent error for mean axial velocity at jet centerline, ucl

Table of Sample percent crior for mean axial velocity at jet conternacy ag				
Axial Location (x/D)	Case 1	Case 2	Case 3	
1.25	4.24	3.70	3.69	
6	3.93	1.63	0.09	
7.5	5.49	3.96	1.40	
9.25	10.46	2.34	1.35	
12.5	10.40	2.29	0.27	

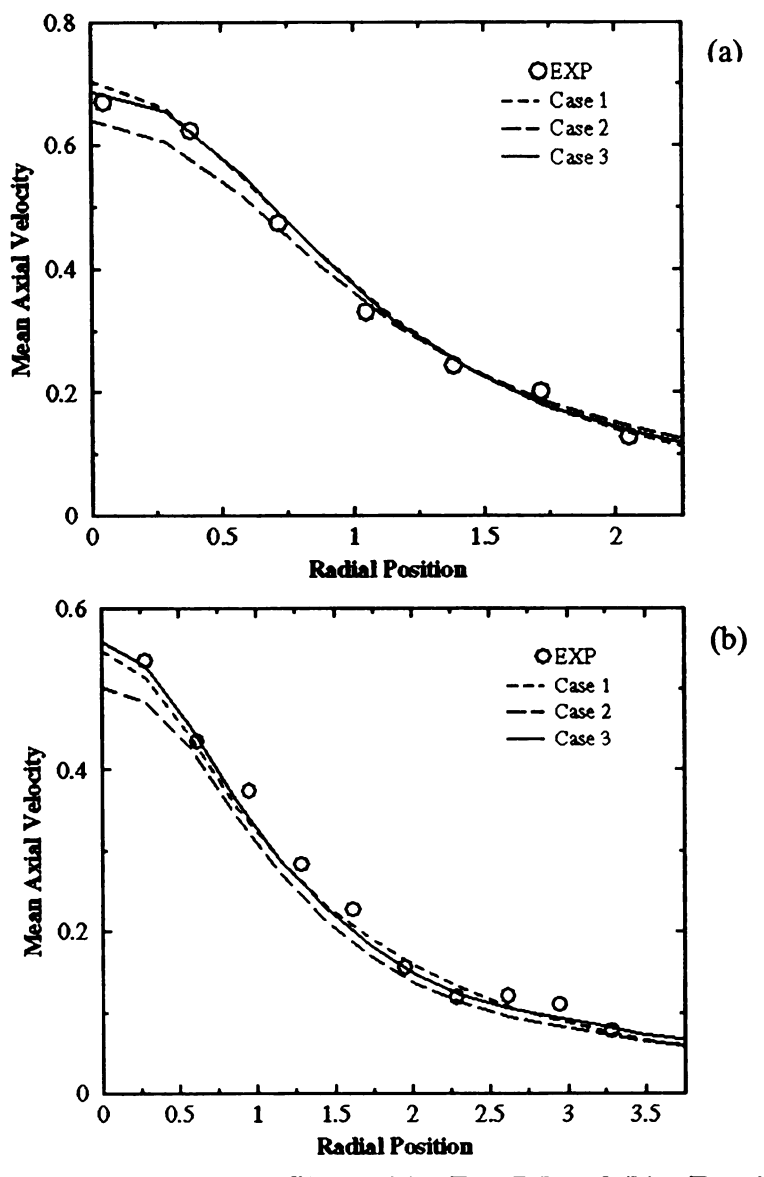


Figure 27. Axial velocity profiles at (a) x/D = 7.5 and (b) x/D = 12.5.

Table 7. Sample percent error for mean axial velocity, um

Axial Location	Radial Location	Case 1 Error	Case 2 Error	Case 3 Error
(x/D)	(r/r _o)	0.42	0.42	0.45
2.5	0.3 1.2	0.42 12.31	0.42 9.72	0.45 11.64
12.5	0.3	9.75	4.16	1.52
12.5	2.3	5.92	9.15	1.56

The spatial development of the velocity field of the carrier gas and dispersed phase for each of the two-phase cases listed in Table 5 is shown in Figure 28. Once again, note the striking similarities between Case 3 and the experimental results. It is easily seen that the LES captures the two-way coupling effects, as there is good agreement for both carrier gas and particle phases.

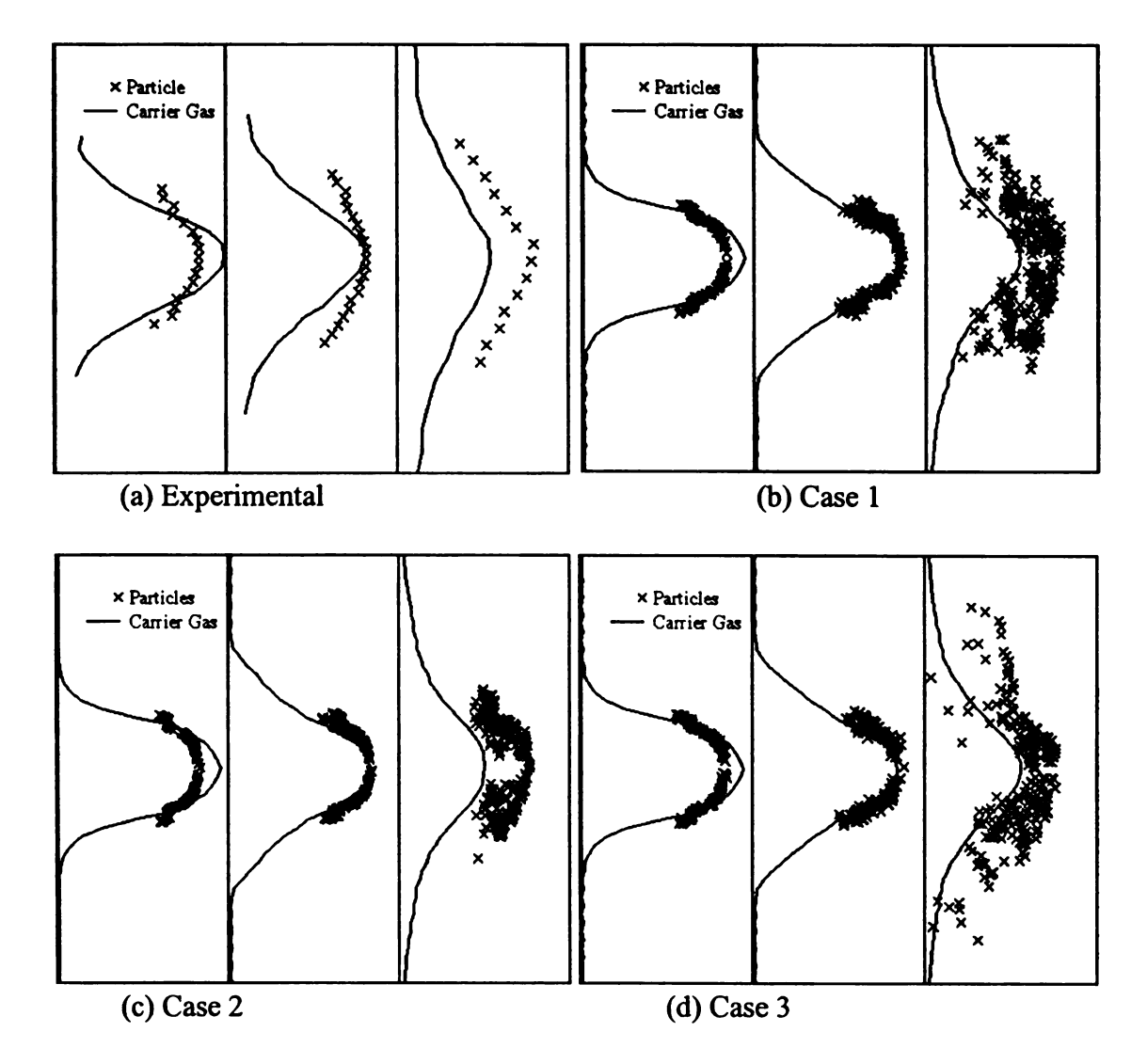


Figure 28. Spatial Development of Axial Velocity Profiles at x/D = 2.5, 5 and 12.5

It is significant to note that the experiment was conducted with relatively large particles,

with $\tau_p = \frac{\rho_p \cdot d_p^2}{18\mu} = 57.4$. This indicates that the particles have a high inertia to drag

force ratio, and tend to follow their own path rather than the path of the fluid (although they still decelerate and grossly affect the carrier gas). It is also important to note that there is a significant variation in the calculation of the radial quantities. The experimental results represent one cross-sectional slice of the jet, while the LES results represent an azimuthally averaged radial profile. Considering the precision of the centerline quantities (where there is no significant difference in sampling), it is not unreasonable to assume that much of the increased errors seen in the radial profiles can be attributed to the difference in sampling between the experimental and LES results. This is mentioned only in an effort to remind the reader that there are fundamental differences in the way that data can be interpreted, especially in the case where there is a significant amount of data that is available for use in calculations. It would be very difficult for an experiment to measure the whole field, whereas the numerical simulation allows for the calculation of the variables at all points in the field.

Figure 29 shows the profiles of the root-mean-square of axial velocity at x/D = 5 and 12.5. Note the significant increase in agreement as the jet develops, indicating that the effects of the two-way coupling are captured with increasing accuracy as the jet develops. It is also an indication that the initial region is highly dependent on the inlet conditions. Table 8 is a collection of various percent errors in the RMS values. Again, notice the increased accuracy of the Case 3 results at farther downstream locations.

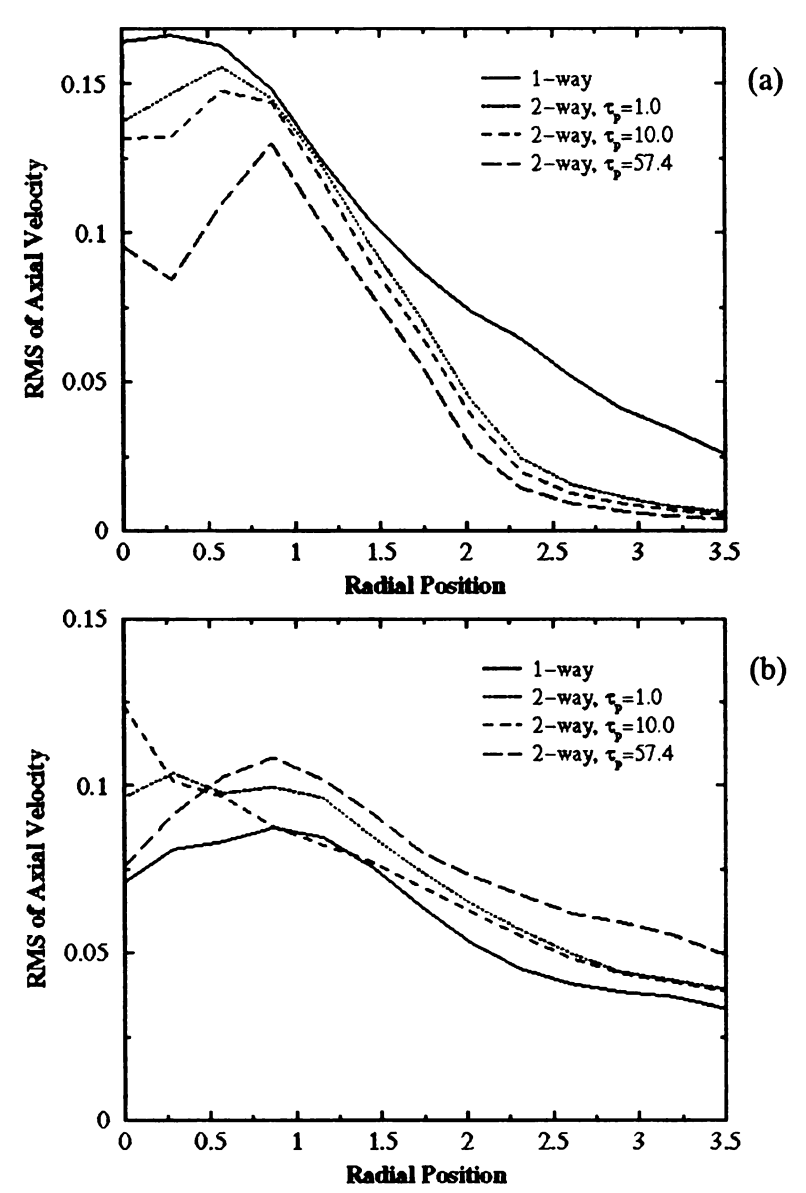


Figure 29. Radial profiles of RMS of axial velocity at (a) x/D = 5 and (b) x/D = 12.5

Table 8. Sample percent error calculations for u_{rms}

Table 8. Sample percent error calculations for urms				
Axial Location	Radial Location	Case 1	Case 2	Case 3
(x/D)	(r/r_o)			
2.5	0.9	20.14	28.27	27.78
5	1.2	21.13	15.93	12.50
12.5	0.3	0.57	22.92	5.81

The last statistical quantity that is examined in this section is the turbulence intensity, Tu.

The turbulence intensity can be calculated as

$$Tu = \frac{u'^2 + v'^2 + w'^2}{\overline{u}^2 + \overline{v}^2 + \overline{w}^2} \cdot 100\%$$
 (18)

Figure 30 shows the radial profiles of the turbulence intensity for the experimental results and the LES results of Case 3 at x/D = 5 and 12.5, and Table 9 gives some sample percent error calculations. Again, it is observed that the LES predictions are in good agreement with the experimental results. It is important to note the relative magnitude of the turbulence intensity; the values are very small, so slight Tu variations cause large error deviations.

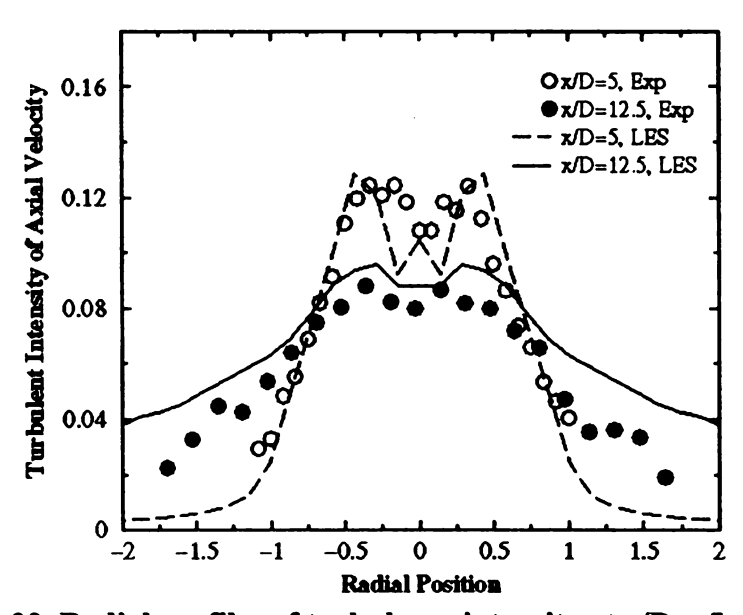


Figure 30. Radial profiles of turbulence intensity at x/D = 5 and 12.5

Table 9. Sample percent error calculations for Tu

Axial Location (x/D)	Radial Location (r/r _o)	Case 1	Case 3
5	0.4	32.8	7.38
5	0	93.7	3.12
12.5	0.9	35.9	7.71
12.5	0.1	22.9	2.05

To further validate the accuracy of the SGS models, comparisons between experimental and LES data are made for the case of single-phase flow. This enables the verification of

the effects of the particles on the carrier gas. As shown in Figures 31 and 32, there is good agreement between both the single- and two- phase flow configurations, a clear indication that the SGS models employed are viable for both. Both the experiment and the simulation show that adding heavy particles to the flow causes the centerline velocity to decay at a slower rate. This can be rationalized in that the heavy particles effectively pull the carrier gas along at their rate, slowing the deceleration due to viscous effects. An increase in turbulence intensity was also noted when particles are added to the flow, which also correlates well with the experimental results.

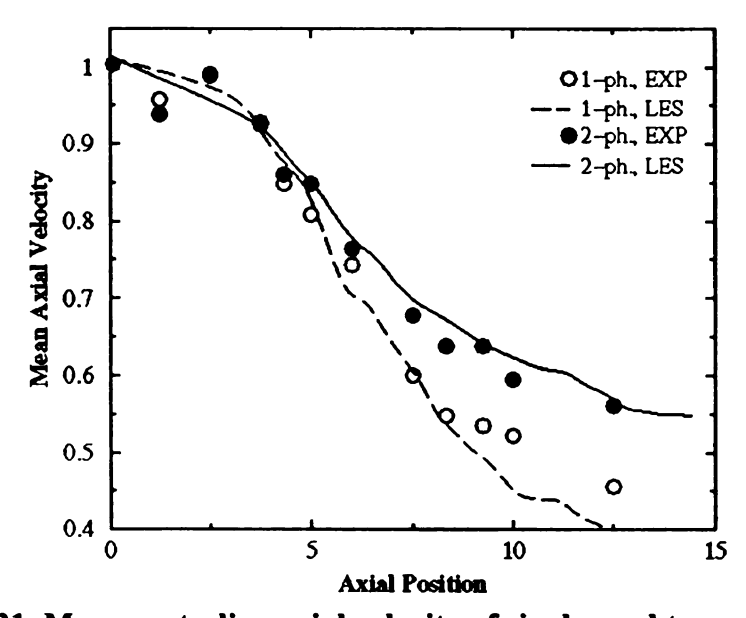


Figure 31. Mean centerline axial velocity of single- and two-phase flow

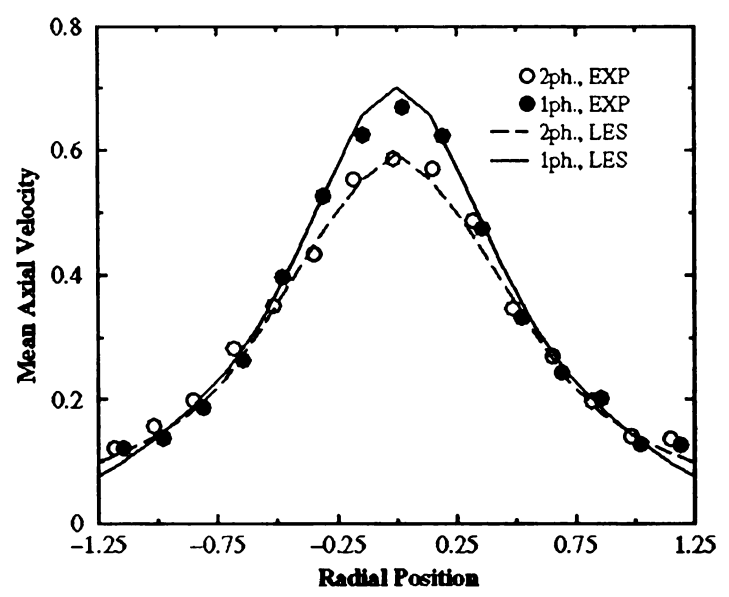


Figure 32. Radial profiles of mean axial velocity at x/D = 7.5

3.2.2 Additional physical observations

In Section 3.2.1, we have validated our LES models and numerical scheme by comparing the numerical results with experimental data. In this section, we use the LES to delve into the physics of two-phase turbulent jet flows. For example, further analysis of the particle number density indicates that the total number of particles integrated over the jet cross-stream direction increases along the jet direction. This is shown in Figure 33 and is due to accumulation, clustering and overall lag of the particles by the particle drag force. The phenomenon can be pictured in other ways as well. Figure 34 shows the velocity of the carrier gas decreasing much more rapidly than the particles. The 'faster' particles near the inlet move downstream quickly, effectively 'catching up' with the particles near the exit plane.

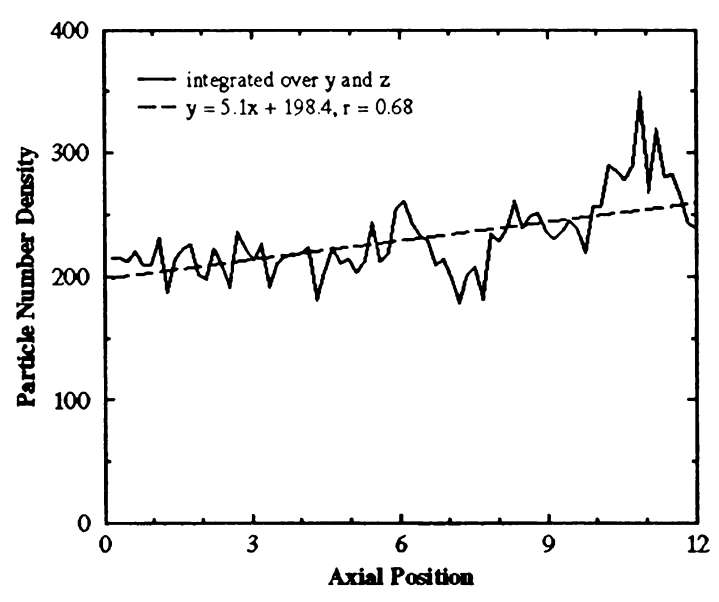


Figure 33. Particle number density versus downstream distance

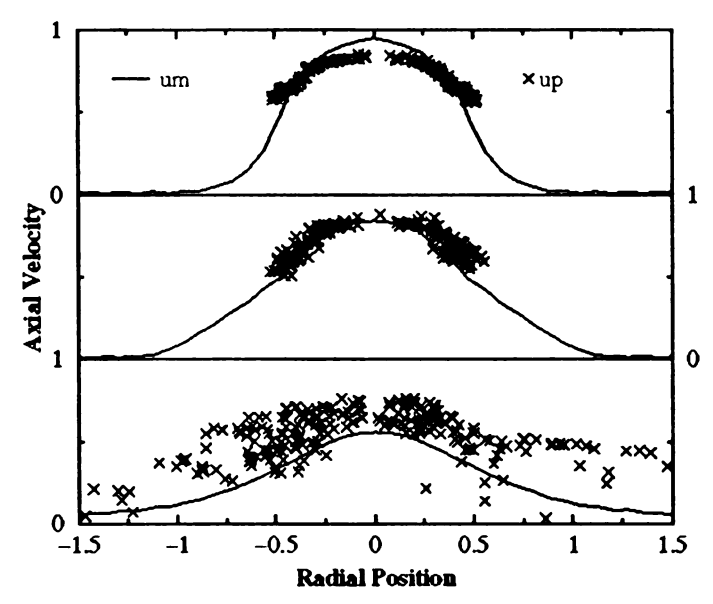


Figure 34. Carrier gas and particle velocity versus radial position at (a) x/D=2.5, (b) x/D=5.0 and (c) x/D=12.5

Figure 35 shows the variation of the particle velocity with particle size or inertia. At the inlet of the jet, the particles are given a velocity that is nearly uniform and close to the local carrier gas velocity. The particle size/mass is randomly chosen and there is no initial correlation between particle mass and location and/or velocity in any way. Farther

downstream, the larger particles tend to stay at their initial velocity, while the smaller particles start to deviate from their initial velocity due to drag effects. Hence, a relationship between the particle mass and velocity can be shown to develop.

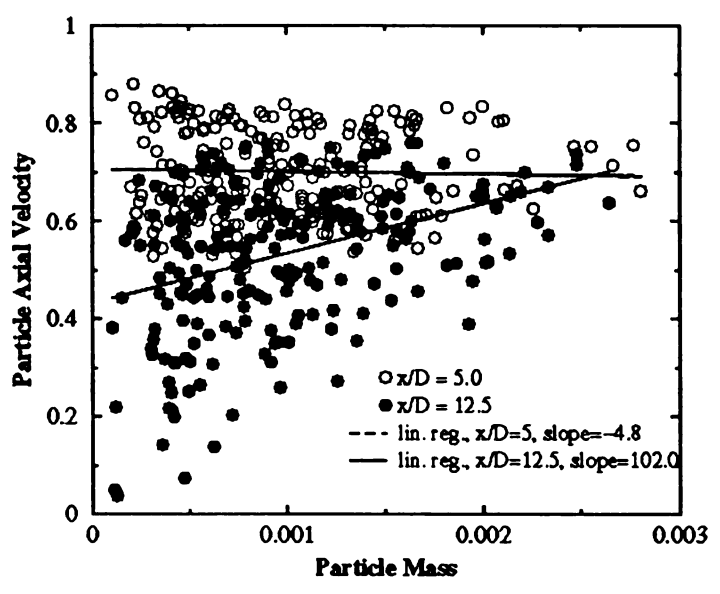


Figure 35. Correlation between particle axial velocity and particle mass at different downstream locations

It is not only the axial velocity of the particles that is affected by the carrier gas. In the LES conducted herein, the initial velocity of the particles is exclusively in the axial direction. If the carrier gas has no effect on particle dispersion, one would expect the particles to remain at their initial (inlet) radial location throughout the jet. Figure 36 shows otherwise. Several of the smaller particles deviate from their original location as they move downstream. This indicates that they must have gained a radial velocity component from the carrier gas two-way interaction drag effects. However, the larger particles tend to remain in the core of the flow. The linear regression shown in the figure is intended to show a general trend, not an empirical relationship.

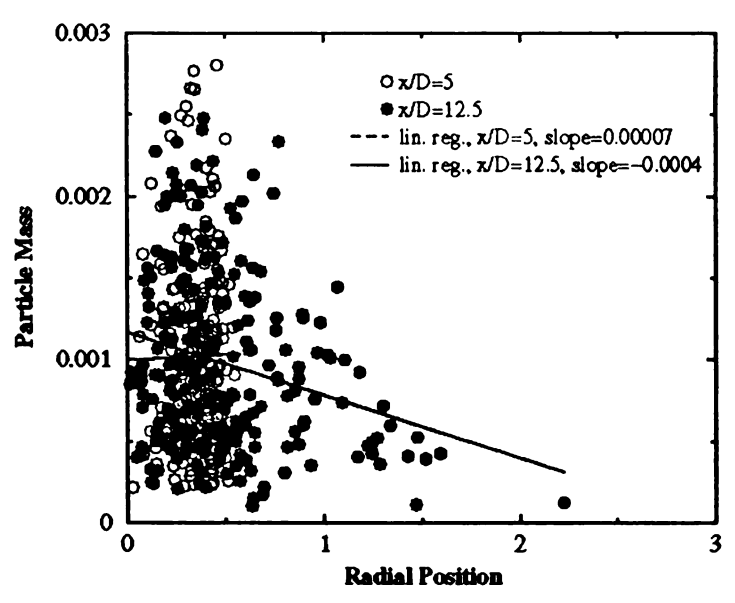


Figure 36. Particle mass versus radial position at different downstream locations

Another way to see the preferential concentration of particles in the jet is to look at a comparison between the particle number density profile and the average particle mass profile, as in Figure 37. The total number of particles entrained in the core of the jet increases in the axial direction, forcing the average particle mass to decline. This does not mean that the larger particles are being replaced by smaller ones. It seems more likely that the average mass is decreasing due only to the addition of smaller particles, not the loss of large particles. This also may be due to the fact that the larger particles are swept downstream at a high velocity while some of the smaller particles are caught in low vorticity regions near the core of the jet. It is interesting to note that there are peaks in the profiles of both the average particle mass and the particle number density near the shear layer. In addition, both plots indicate that there is noticeable particle dispersion for the x/D=12.5 location, as evidenced by the smaller peaks beyond r/D=0.7.



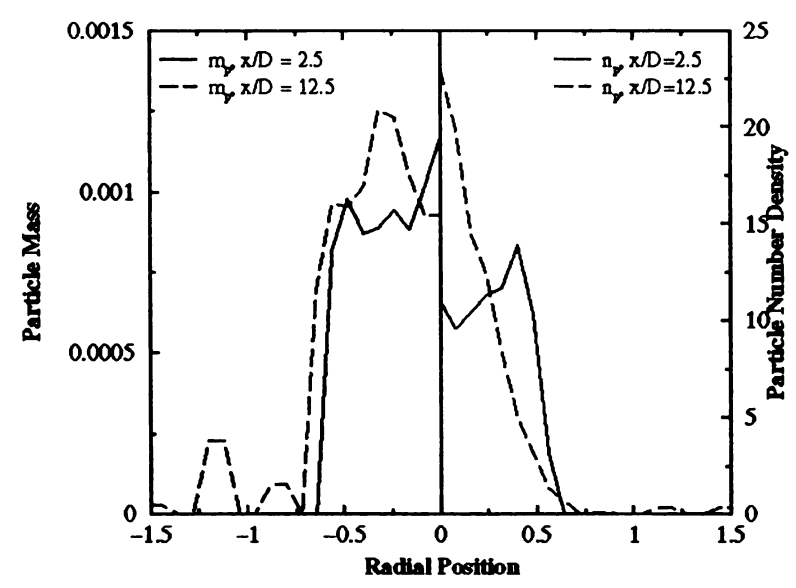


Figure 37. Particle mass and number density radial variation at different axial locations

The clipped Gaussian particle size distribution applied at the inlet of the jet was with respect to the particle diameter. The probability distribution of the particle size by mass is shown in Figure 38. Of particular interest is the positive skewness of the pdf, indicating that there are more excursions from the mean on the larger particle side. This distribution remains nearly constant at different axial locations. The pdfs are integrated over the entire plane perpendicular to the jet; so local particle distribution is not distinct, only general axial trends.

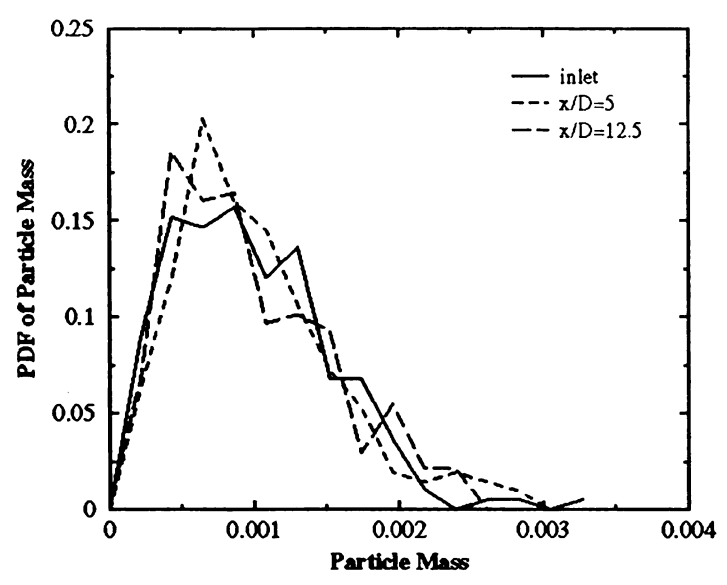


Figure 38. Probability distribution function of particle mass

Velocity correlations can be very insightful as to the physics of two-phase jet flows. One can see how carrier gas production, transport and dissipation are affected by the particle phase by looking at particular correlations. In the computation of a two-phase jet, different correlations become available and relevant. Consider Figure 39, which shows the axial variation of the particle-carrier gas velocity correlations, which are integrated over the plane perpendicular to the jet at each axial location. The correlation between the axial velocities of the carrier gas and the particles, $\overline{u_p u^*}$, where the asterisk (*) again denotes the carrier gas property interpolated to the particle position, is the most significant, meaning that the ability to predict the carrier gas axial velocity knowing the particle axial velocity is better than the other velocity correlations. The velocity correlations decay along the axial direction as expected, indicating that there is increased randomness in the slip velocity farther downstream than there is in the near-field. Also, the radial components of the particle and carrier gas velocities are not very well

correlated $(v_p v^* \approx 0)$, while the cross-correlations, $u_p v^*$ and $v_p u^*$, are both the same.

They are opposite in sign of $u_p u^*$ and of lower magnitude.

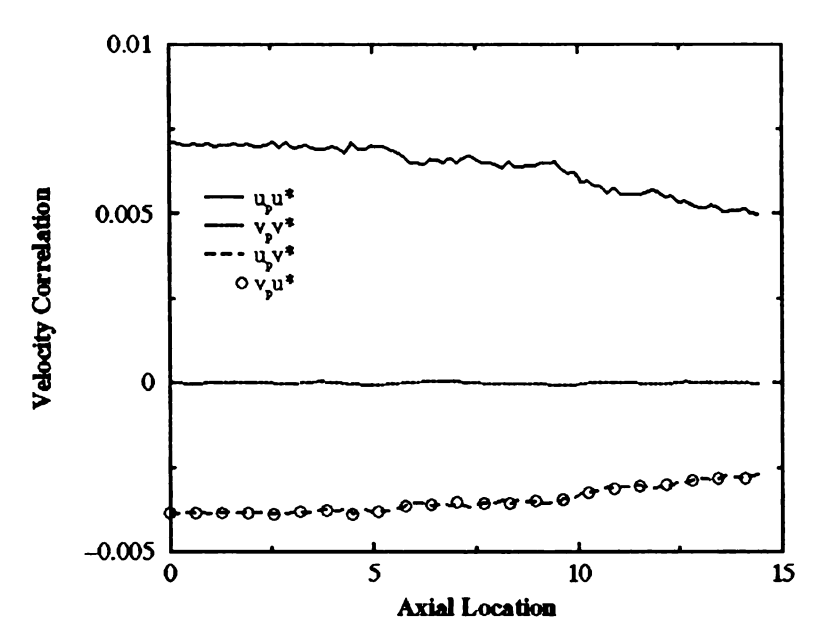


Figure 39. Axial variation of correlation between particle and carrier gas velocities

Figure 40 shows the same velocity correlations as Figure 39, but here the focus is on the radial variation of the velocity particle-carrier gas correlation, as the correlations are integrated over the jet length for each radial location. The sharp peaks appearing farther away from the centerline are caused by a low particle density in those regions. There are interesting differences between the axial variation and the radial variations. The $\overline{u_p u}^*$ correlation is still the most significant and the $\overline{v_p v}^*$ correlation is still very poor. However, the $\overline{u_p v}^*$ and $\overline{v_p u}^*$ are no longer equal, and it seems as though the $\overline{u_p u}^*$ is balanced by the $\overline{u_p v}^*$. A portion of the disparity in Figures 39 and 40 can be attributed to the integration; the particle dispersion

effects are not accounted for on a local level when the correlations are integrated over the entire jet length or cross-plane. Additionally, the sample size varies greatly in regions of low particle concentrations. Figure 40 implies that the particle axial velocity correlates well with both components of the carrier gas velocity, whereas the radial velocity of the carrier gas has minimal correlation with either component of the carrier gas. Recall that the particles considered in this study are quite large, and that they are not given any radial component of velocity initially. Any radial velocity that they obtain is thus very small and somewhat random, which helps to explain the observed low correlation. It is interesting that the radial velocity of the carrier gas correlates with the axial velocity of the particles better than it does with the radial velocity of the particles when integrated over the length of the jet, as in Figure 40. Conversely, it is equally as interesting that the two cross-correlations are nearly identical when integrated over the jet cross-plane, as in Figure 39.

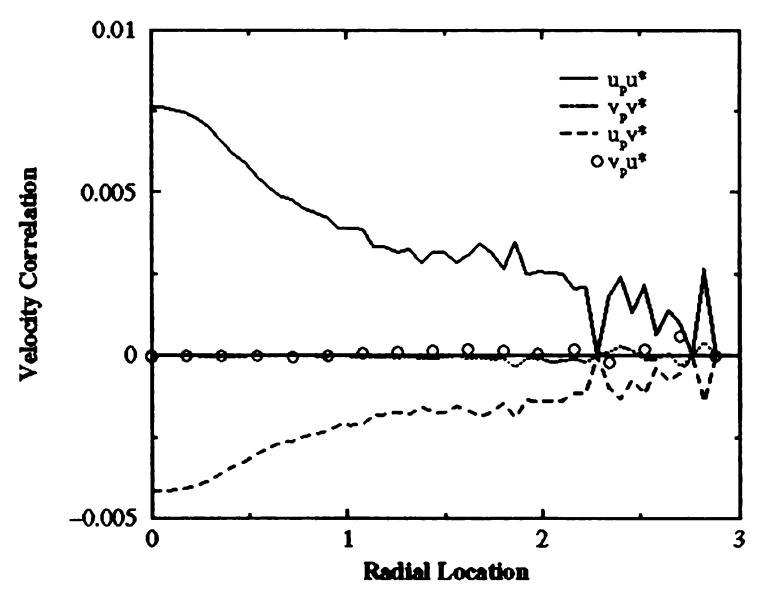


Figure 40. Radial variation of correlation between particle and carrier gas velocities

One of the more difficult problems facing experimentalists is that of accurately resolving both temperature and velocity fields of highly turbulent flows. Figure 41 can be used to gain some insight about the thermal inertia of the particles. It is obvious that the larger particles will respond to the flow in quite different ways than the smaller ones. Not only will they act as larger momentum sources and sinks, but they will also act as thermal sources and sinks. As the smallest scales of turbulence are dissipated into the internal energy of the carrier gas, a significant part of that energy will be transferred to the particles (1998a). Figure 41 shows that the temperature distribution of the smaller particles will, in fact, spread out as the jet develops. In the near field, all particles are at nearly the same temperature, while further downstream the smaller particles attain higher temperatures in comparison to the larger ones. This can affect the carrier gas temperature field and, for sufficiently large temperature variations, the fluctuating velocity field.

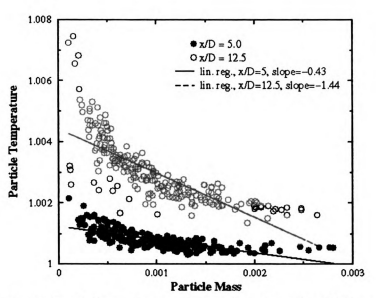


Figure 41. Particle temperature as a function of particle mass

The results shown in Figures 33-41 are for particles with relatively large average τ_p , similar to that in the experiment. Experimentally, it is difficult to consider smaller particles due to the interference of the particle phase with the seeded particles. It is not however very difficult to perform numerical simulations with smaller average τ_p . Figure 42 shows the difference in the root-mean-square of axial velocity of the carrier phase due to the introduction of different average particle sizes. The figure shows that the attenuation of the turbulence is greater for the cases with larger average particle sizes.

Figure 43 is further evidence that the size of the particles in two-phase jets can be very important and should never be neglected. It is a plot of the mean axial velocity versus axial position at the centerline and versus radial position at x/D = 7.5. Note that in (a) the effects of the particles are minimized by decreasing their size. This is due to the inlet conditions imposed upon both phases. In all three two-phase cases, the particles are initialized at a velocity that is less than that of the carrier gas. In the cases with larger

particles, the particles have a large inertia, and effectively drag the carrier gas along at their velocity, while the smaller particles generally interact in a more complicated way.

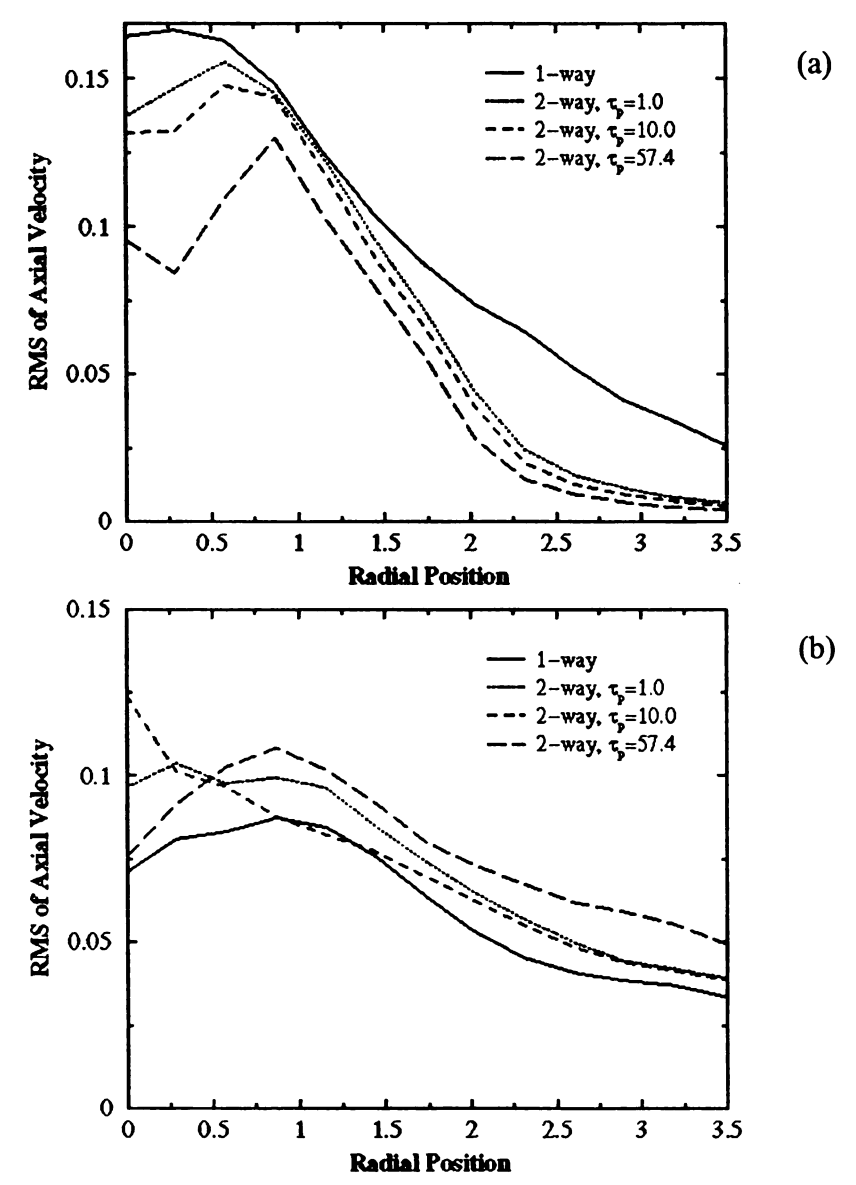


Figure 42. Mean axial velocity versus radial position for varying average particle inertia at (a) x/D = 5 and (b) x/D = 12.5

The smallest particles appear to have no effect on the mean flow, while the larger particles significantly decrease the decay of the centerline velocity. The plot of radial variation of axial velocity can be interpreted in a similar way. The smaller particles seem

to augment the axial velocity at this particular axial location, while the larger particles seem to attenuate the carrier gas velocity.

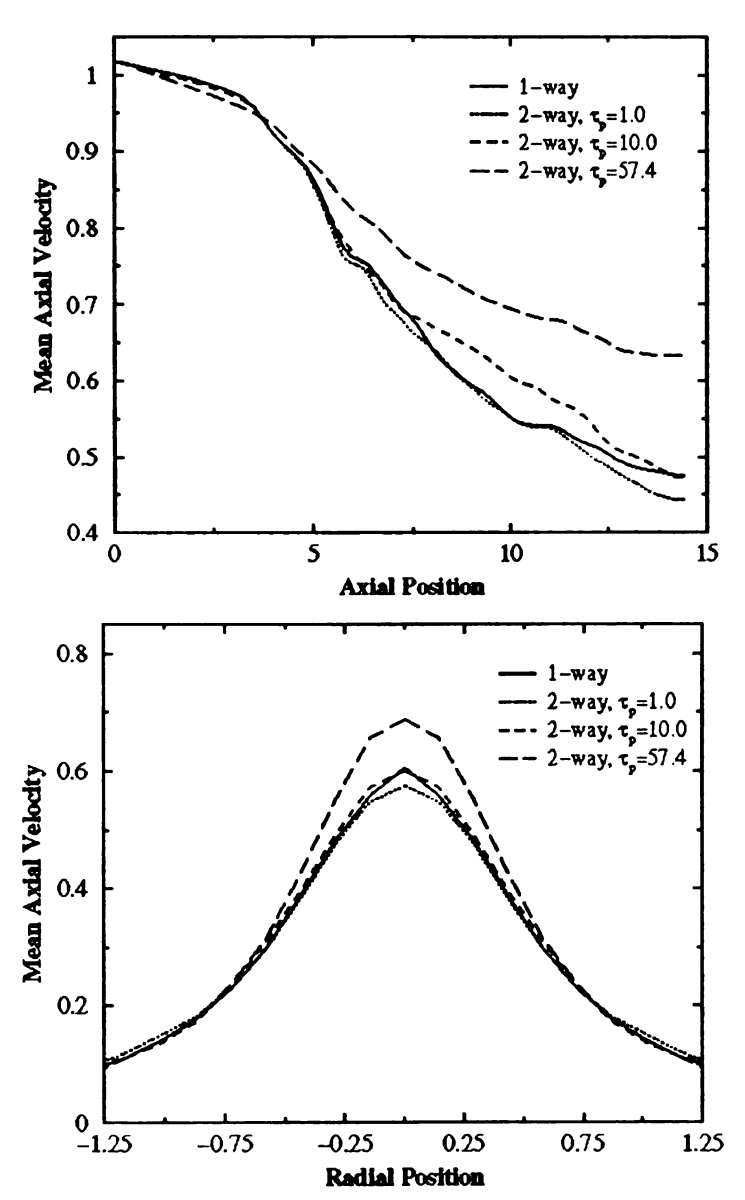


Figure 43. Mean axial velocity (a) versus axial position at the centerline and (b) versus radial position at x/D = 7.5

CHAPTER 4CONCLUSIONS

In Chapter 2, direct numerical simulations (DNS) of two-dimensional, droplet-laden, harmonically forced jets were conducted in an effort to better understand the underlying physics involved in such flows. Full two-way mass, momentum and energy coupling between phases was considered. The effects of particle time constant, carrier gas temperature and 'degrees of coupling' on various turbulent properties were numerically measured.

The results indicate that the downstream particle dispersion is nearly independent of particle injection for one-way coupling cases. The previous findings related to particle size and preferential concentration were confirmed, as smaller particles tend to follow the flow and therefore do not preferentially concentrate, while larger particle are largely unaffected by the carrier gas and also do not preferentially concentrate. The phenomenon of local particle dispersion was noted, as moderately sized particles tend to cluster together in regions of low-strain, while either large or small particles tend to spread out in the flow (by their own large- or small-particle mechanisms).

The cases for two-way coupled, non-evaporating droplets indicate that temperature effects are still very significant. The finite thermal inertia of the particles significantly alters the density profile of the jet, causing a modification of the instabilities that govern jet growth rate. Thus, cooler particles injected into a hot jet will tend to stabilize the jet, decreasing the growth rate. In addition to temperature effects, the effects of mass loading

were investigated. The results indicate that as the mass-loading ratio increases, the slope of the jet half-width increases as well. This relationship is hypothesized to be linear for the range of mass loading ratios considered in this study. The results also indicate that the production of turbulent kinetic energy is greatly affected by the presence of solid particles (and also evaporating droplets). The production of turbulent kinetic energy (TKE) was found to be of opposite sign on the positive transverse side of the jet, indicating a significant sink of TKE due to the particles. The relative magnitude of the Reynolds stress was found to decrease with increased mass loading.

Perhaps the most valuable findings are those of the evaporating cases. An effort has been made to clearly separate the turbulence modification due to temperature effects, particle drag and heat transfer and evaporative effects (e.g., added mass). Evaporative effects contributed to the increased stability of the jets in this study, as the evaporation decreased the temperature and increased the density of the carrier gas. The Reynolds stress was damped by the addition of the evaporation mechanism. Hence, the production of TKE was also decreased. By considering the most physically complicated case, the effects of interpolation scheme on solution accuracy were determined to be insignificant.

The long-range goal of this and other similar works is to accurately predict the behavior of multiphase turbulent flows in complex geometries using numerical methods. This study is part of a larger ongoing effort to develop more accurate and robust turbulence closure models. Specifically, the DNS results (for these two-dimensional and future three-dimensional cases) will be used in *a priori* analyses to develop sub-grid scale

(SGS) closure models for the large-eddy simulation (LES) methods of computing multiphase turbulent flows. The full analysis of the three-dimensional results will be the subject of future work.

In Chapter 3, the abilities of large eddy simulation (LES) methods to predict multiphase turbulent flows was investigated via an *a posteriori* study, correlating experimental and numerical results for an axisymmetric turbulent round jet laden with heavy particles. The results indicate that the subgrid-scale (SGS) carrier gas stress model and stochastic SGS model employed for particles in the LES are viable and the latter increase the accuracy of the numerical prediction by as much as 10%. Three different simulations of the flow were conducted. Of these, the simulation utilizing both the stochastic particle SGS model and the non-uniform (Gaussian) particle size distribution (Case 3) most accurately predicted the various measured turbulent quantities, while the simulation that did not incorporate either of these two (Case 1) was the least precise. The simulation that included the SGS particle model but not the Gaussian particle size distribution (Case 2) was reasonably accurate, but less so than the previously mentioned Case 3. In addition to the results for two-phase flow, results were considered for the single-phase flow, for which the LES utilizing the SGS closures was also accurate.

Additional results indicated that the physics of the two-phase round jet are complex indeed. How the particles affect the turbulent velocity field and the thermal field leads to interesting connections between the two. The results indicate that as the carrier gas velocity fluctuations are damped by the particles the dissipation decreases, but the

particle temperature increases, showing a true two-way coupling effect. The analysis of the thermal inertia of particles shows that the temperature distribution of the small particles widens as the jet develops, while the temperature distribution of the large particles remains nearly constant. The velocity distribution of the particles follows a similar pattern, as expected. The larger particles tend to keep their initial velocity, while the smaller particles tend to accelerate and/or decelerate more readily, and thus have a more disperse correlation between mass and velocity. Analysis of particle number density and average particle mass profiles supports these findings.

Analysis of the probability distribution functions of the particle mass indicates that the size density remains relatively the same in the axial direction of the flow. Analysis of the particle-carrier gas velocity correlations indicate that they decay in the axial and the outward radial directions, leading to increased slip velocities in those locations. Interestingly, the axial velocity correlations do not follow the same trends as the radial velocity correlations. Both indicate that the dominant correlation is the correlation between the axial velocities of the carrier gas and the particles, and that the correlation between the radial velocities of the carrier gas and the particles is approximately zero. However, the correlations integrated over the plane perpendicular to the jet indicate that both the cross-correlations are similar, whereas the correlations integrated over the length of the jet indicate that the correlation between the axial velocity of the particles and the radial velocity of the carrier gas is significant, and the correlation between the radial velocity of the particles and the axial velocity of the carrier gas is minimal.

Further analysis based on modifying the average particle inertia indicates that the choice of particle size can significantly affect the turbulence fields of two-phase jets. The growth of the jet can be amplified with the addition of tiny (micro-) particles, or greatly attenuated with the addition of very large particles to the flow. It has been shown that the numerical simulation of two-phase jets using LES methods is an efficient and accurate method to conduct experiments in order to help to determine real physical parameters that govern a particle-laden flow.

REFERENCES

REFERENCES

- Aísa, L, Garcia, J, Cerecedo, L, García Palacín, I. and Calvo, E. (2002). Particle concentration and local mass flux measurements in two-phase flows with PDA. Application to a study on the dispersion of spherical particles in a turbulent air jet. International Journal of Multiphase Flow. vol. 28, pp. 301-324.
- Armenio, V. and Fiorotto, V. (2001). The importance of the forces acting on particles in turbulent flows. <u>Physics of Fluids</u>. vol. 13, no. 8, pp. 2437-2440.
- Armenio, V, Piomelli, U. and Fiorotto, V. (1999). Effect of the subgrid scales on particle motion. <u>Physics of Fluids</u>. vol. 11, no. 10, pp. 3030-3042.
- Baum, M, Poinsot, T. and Thevenin, D. (1994). Accurate boundary conditions for multicomponent reactive flows. <u>Journal of Computational Physics</u>. vol. 116, pp. 247-261 (1994).
- Bellan, J. (2000). Perspectives on large eddy simulations for sprays: Issues and solutions. Atomization and Sprays. vol. 10, pp. 409-425.
- Bernard, P. and Wallace, J. (2002). <u>Turbulent Flow</u>. Hoboken, New Jersey: John Wiley & Sons, Inc.
- Boivin, M, Simonin, O. and Squires, K. (1998). Direct numerical simulation of turbulence modulation by particles in isotropic turbulence. <u>Journal of Fluid Mechanics</u>. vol. 375, pp. 235-263.
- Boivin, M, Simonin, O. and Squires, K. (2000). On the prediction of gas-solid flows with two-way coupling using large eddy simulation. <u>Physics of Fluids</u>. vol. 12, no. 8, pp. 2080-2090.
- Colucci, P. (1994). Linear stability analysis of density stratified parallel shear flows. 32nd Areospace Sciences Meeting & Exhibit. AIAA-94-0011.
- Crowe, C, Chung, J. and Troutt, T. (1988). Particle mixing in free shear flows. <u>Progress in Energy and Combustion Science</u>. vol. 14, pp. 171-194.
- Eaton, J. and Fessler, J. (1994). Preferential concentration of particles by turbulence. <u>International Journal of Multiphase Flow</u>. vol. 20, suppl, pp. 169-209.
- Elghobashi, S. and Truesdell, G. (1993). On the two-way interaction between homogeneous turbulence and dispersed solid particles. I: Turbulence modification. <u>Physics of Fluids A</u>. vol. 5, no. 7, pp. 1790-1801.

- Fan, L. and Zhu, C. (1998). <u>Principles of Gas-Solid Flows</u>. New York, New York: Cambridge University Press.
- Ferrante, A. and Elghobashi, S. (2003). On the physical mechanisms of two-way coupling in particle-laden isotropic turbulence. <u>Physics of Fluids</u>. vol. 15, no. 2, pp. 315-329.
- Gillandt, I, Fritsching, U. and Bauckhage, K. (2001). Measurement of phase interaction in dispersed gas/particle two-phase flow. <u>International Journal of Multiphase Flow</u>. vol. 27, pp. 1313-1332.
- Hansell, D, Kennedy, I. and Kollmann, W. (1992). A simulation of particle dispersion in a turbulent jet. <u>International Journal of Multiphase Flow</u>. vol. 18, no. 4, pp. 559-576.
- Hinze, J. (1975). Turbulence. New York, New York: McGraw-Hill.
- Hsiao, F. and Huang, J. (1990). On the evolution of instabilities in the near field of a plane jet. Physics of Fluids A. vol. 2, no. 3, pp. 400-412.
- Jaberi, F. (1998). Temperature fluctuations in particle-laden homogeneous turbulent flows. International Journal of Heat and Mass Transfer. vol. 41, pp. 4081-4093.
- Jaberi, F. (2000). Temperature decay in two-phase turbulent flows. <u>International Journal of Heat and Mass Transfer</u>. vol. 43, pp. 993-1005.
- Jaberi, F. and Colucci, P. (2003). Large eddy simulation of heat and mass transport in turbulent flows. Part I: Velocity field. <u>International Journal of Heat and Mass Transfer</u>. vol. 46, pp. 1811-1825.
- Kennedy, C. and Chen, J. (1998). Mean flow effects on the linear stability of compressible planar jets. <u>Physics of Fluids</u>. vol. 10, no. 3, pp. 615-626.
- Kennedy, I. And Moody, M. (1998). Particle dispersion in a turbulent round jet. Experimental Thermal and Fluid Science. vol. 18, pp. 11-26.
- Ling, W, Chung, J. and Crowe, C. (2001). Direct numerical simulation of a two-way thermally coupled droplet-laden mixing layer. <u>Journal of Fluid Mechanics</u>. vol. 437, pp. 45-68.
- Longmire, E. and Eaton, J. (1992). Structure of a particle-laden round jet. <u>Journal of Fluid Mechanics</u>. vol. 236, pp. 217-257.
- Mashayek, F. (1998a). Droplet-turbulence interactions in low-Mach-number homogeneous shear two-phase flows. <u>Journal of Fluid Mechanics</u>. vol. 367, pp. 163-203.

- Mashayek, F. (1998b). Direct numerical simulations of evaporating droplet dispersion in forced low Mach number turbulence. <u>International Journal of Heat and Mass Transfer</u>. vol. 41, no. 17, pp. 2601-2617.
- Mashayek, F. and Jaberi, F. (1999). Particle dispersion in forced isotropic low-Machnumber turbulence. <u>International Journal of Heat and Mass Transfer</u>. vol. 42, pp. 2823-2836.
- Mashayek, F. (2000). Numerical investigation of reacting droplets in homogeneous shear turbulence. <u>Journal of Fluid Mechanics</u>. vol. 405, pp. 1-36.
- Mashayek, F. and Jaberi, F. (1999). Particle dispersion in forced isotropic low-Mach number turbulence. <u>International Journal of Heat and Mass Transfer</u>. vol. 42, pp. 2823-2836.
- Michaelides, E. (1997). Review The transient equation of motion for particles, bubbles and droplets. <u>Journal of Fluids Engineering</u>. vol. 119, pp. 233-247.
- Miller, R. (2001). Effects of nonreacting solid particle and liquid droplet loading on an exothermic reacting mixing layer. <u>Physics of Fluids</u>. vol. 13, no. 11, pp. 3303-3320.
- Miller, R. and Bellan, J. (1999). Direct numerical simulation of a confined three dimensional gas mixing layer with one evaporating hydrocarbon-droplet-laden stream. <u>Journal of Fluid Mechanics</u>. vol. 384, pp. 293-338.
- Miller, R. and Bellan, J. (2000). Direct numerical simulation and subgrid analysis of a transitional droplet laden mixing layer. <u>Physics of Fluids</u>. vol. 12, no. 3, pp. 650-671.
- Miller, R, Harstad, K. and Bellan, J. (1998). Evaluation of equilibrium and non equilibrium evaporation models for many-droplet gas-liquid flow simulations. <u>International Journal of Multiphase Flow.</u> vol. 24, pp. 1025-1055.
- Ooms, G. and Jansen, G. (2000). Particles-turbulence interaction in stationary, homogeneous, isotropic turbulence. <u>International Journal of Multiphase Flow.</u> vol. 26, pp. 1831-1850.
- Poinsot, T. and Lele, S. (1992). Boundary conditions for direct simulations of compressible viscous flow. <u>Journal of Computational Physics</u>. vol. 101, pp. 104-129.
- Pope, S. (2000). Turbulent Flows. New York, New York: Cambridge University Press.

- Prevost, F, Boree, J, Nuglisch, H. and Charnay, G. (1994). Characterization of a polydispersed particle-laden jet using a phase Doppler anemometer. <u>Proceedings of ICLASS</u>. pp. 938-45.
- Rudy, D. and Strikewerda, J. (1980). A nonreflecting outflow boundary condition for subsonic Navier-Stokes calculations. <u>Journal of Computational Physics</u>. vol. 36, pp. 55-70.
- Schreck, S. and Kleis, S. (1993). Modification of grid-generated turbulence by solid particles. <u>Journal of Fluid Mechanics</u>. vol. 249, pp. 665-88.
- Stanley, S. and Sarkar, S. (1997). Simulations of spatially developing two-dimensional shear layers and jets. <u>Theoretical and Computational Fluid Dynamics</u>. vol. 9, pp. 121-147.
- Tsuji, Y, Morikawa, Y, Tanaka, T, Karimine, K. and Nishida, S. (1988). Measurement of an axisymmetric jet laden with coarse particles. <u>International Journal of Multiphase Flow</u>. vol. 14, pp. 565-74.
- Yang, C. and Lei, U. (1998). The role of the turbulent scales in the settling velocity of heavy particles in homogeneous isotropic turbulence. <u>Journal of Fluid Mechanics</u>. vol. 371, pp. 179-205.
- Yuu, S, Ueno, T. and Umekage, T. (2001). Numerical simulation of the high Reynolds number slit nozzle gas-particle jet using subgrid-scale coupling large eddy simulation. Chemical Engineering Science. vol. 56, pp. 4293-4307.

